1   Revision 1, Word Count: 9,766

2   **Structure of basaltic glass at pressures of up to 18 GPa**

3

4   TOMONORI OHASHI[1,*], TATSUYA SAKAMAKI[1], KEN-ICHI FUNAKOSHI[2], TAKANORI HATTORI[3],

5   NAOKI HISANO[1], JUN ABE[2], AND AKIO SUZUKI[1]

6   [1]Department of Earth Science, Graduate School of Science, Tohoku University, Sendai, 980-

7   8578, Japan

8   [2]Neutron Science and Technology Center, Comprehensive Research Organization for Science

9   and Society (CROSS), Ibaraki, 319-1106, Japan

10   [3]J-PARC Center, Japan Atomic Energy Agency, Ibaraki, 319-1195, Japan

11

12   * Corresponding author, E-mail: tomonori.ohashi.s8@dc.tohoku.ac.jp

13

14   **ABSTRACT**

15   The structures of cold-compressed basaltic glass were investigated at pressures of up to 18

16   GPa using in situ X-ray and neutron diffraction techniques to understand the physicochemical

17   properties of deep magmas. On compression, basaltic glass changes its compression behavior: the

18   mean O-O coordination number (CN_{OO}) starts to rise with maintaining the mean O-O distance (r_{OO})

19   above about 2–4 GPa, and then CN_{OO} stops increasing and r_{OO} begins to shrink along with the

20   increase in the mean coordination number of Al (CN_{AlO}) above approximately 9 GPa. The change

21   around 9 GPa is interpreted by the change in the contraction mechanism from bending tetrahedral

22   networks of glass to increasing oxygen packing ratio via the increase in CN_{AlO}. The analysis of the

23   oxygen packing fraction (η_O) under high pressure revealed that η_O exceeds the value for dense

24   random packing, suggesting that the oxygen-packing hypothesis recently proposed cannot account

25   for the pressure-induced structural transformations of silica and silicate glasses. The rise of the

26   CN_{OO} at 2–4 GPa reflects the elastic softening of fourfold-coordinated silicate glass, which may be

27   the origin of anomalies of elastic moduli in basaltic glass at ~2 GPa previously reported by Liu and

28   Lin (2014).

29   The widths of both the first sharp diffraction peak and the principal peak show contrastive

30   compression behaviors between modified silicate and silica glasses. This result suggests that

31   modified silicate glasses represent different pressure evolutions in the ranges of the intermediate-

32   and the extended-range order structures from those of silica glass, likely due to the presence of

33   modifier cations and the resultant formations of smaller rings and cavity volume.

34

35   **Keywords:** Glass structure, permanent densification, high pressure, X-ray diffraction, neutron

36   diffraction

37

38   **INTRODUCTION**

39   It is well known that the physicochemical properties of magmas, such as density, viscosity,

40   and elastic moduli, are sensitive to their atomic structures (e.g., Sakamaki 2018). Thus, the

41   structural change under high pressure attracted considerable interests. Although it is important to

42   explore the macroscopic properties and structures of silicate melts at high pressures and

43   temperatures, many technical challenges are involved in performing in situ experiments of melts

44   under extreme conditions. Glasses, which can be a quenched form of the liquid, are believed to

45   show a similar behavior; thus, numerous studies on the glasses have been undertaken to better

46   understand the physical properties of silica and silicate melts under pressure (e.g., Meade and

47   Jeanloz 1988; Sato and Funamori 2008; Liu and Lin 2014). A considerable number of experiments

48   aimed at determining high-pressure structures of silica and silicate glasses have also been

49   conducted by X-ray diffraction, XRD (e.g., Sato and Funamori 2010; Kono et al. 2018; Ohashi et

50   al. 2018), and neutron diffraction, ND (e.g., Wilding et al. 2012; Zeidler et al. 2014a; Salmon et al.

2

51   2019).

52   From these studies, silica and silicate glasses are believed to exhibit two types of states under

53   pressure. The first one is characterized by the fourfold-coordinated ordinary glass, which contracts

54   the intermediate-range order (IRO) structure, at pressures below ~10–20 GPa (e.g., Wang et al.

55   2014; Sanloup 2016; Petitgirard et al. 2019). The second one is characterized by the highly

56   coordinated state above ~40–60 GPa (e.g., Benmore et al. 2010, 2011; Sato and Funamori 2010;

57   Prescher et al. 2017; Petitgirard et al. 2019). Between these states, the Si(Al)-O coordination

58   number gradually increases from 4 to 6. Recent ab initio molecular dynamics (MD) simulation

59   studies (Ghosh et al. 2014; Ghosh and Karki 2018) have also predicted these states. Irreversible

60   structural changes in SiO_2 glass at room temperature has led to the proposition that permanently

61   densified SiO_2 glass exhibits different decompression behavior from that of ordinary SiO_2 glass and

62   the decompression behavior varies with the highest pressure applied (Grimsditch 1984;

63   Vandembroucq et al. 2008). This densified state was interpreted by Wakabayashi et al. (2011) as a

64   mixture of low- and high-pressure IRO structures. The high-pressure IRO component is composed

65   of small Si-O-Si rings (Zeidler et al. 2014a; Ryuo et al. 2017) and inter-tetrahedral voids (Wilding

66   et al. 2012; Zanatta et al. 2014) compared to the low-pressure state.

67   According to previous studies, the structure of network-forming glass/melt is expressed by the

68   order in three characteristic scales: the short-, intermediate-, and extended-range orders. The short-

69   range order refers to correlations between the nearest neighbors. The intermediate- and extended-

70   range orders (EROs) are related to correlations at distances longer than the nearest neighbor.

71   Previous studies (e.g., Zachariasen 1932; Price et al. 1997; Mei et al. 2008) have shown that, in

72   silica, germania, and germanate glasses, the IRO originates from atomic density fluctuations in the

73   networks formed by connections between SiO_4/GeO_4 tetrahedral units. The periodicity of IRO is

74   related to a first sharp diffraction peak (FSDP) in the structure factor, $S(Q)$ (e.g., Price et al. 1988;

75   Elliott 1991; Wright 1994; Mei et al. 2008). Previous ND experiments have demonstrated that a

76   contribution from the second peak (principal peak, PP) is associated with the extended-range

77   ordering and packing of structural building blocks (Salmon et al. 2005, 2006; Salmon 2018).

78   Another interpretation of the PP argued that it originates from the local order of tetrahedra (Shi and

79   Tanaka 2019).

80   Basalt is the archetypal composition of natural silicate melts and is produced abundantly at the

81   surface of the Earth. Previously, the structure of ambient basaltic glass was examined by an XRD

82   (Drewitt et al. 2013) and a nuclear magnetic resonance, NMR (Park and Lee 2018) studies.

83   However, the pressure effect on the structure was not explored. Ohashi et al. (2018) conducted

84   high-pressure XRD experiments on cold-compressed basaltic glass up to 6.0 GPa. In their study,

85   basaltic glass showed the contraction of the IRO structure without increasing the mean Si(Al)-O

86   coordination number. As reported by previous XRD experiments (Drewitt et al. 2015) and MD

87   simulations (Drewitt et al. 2015; Ghosh and Karki 2018) on $CaAl_2Si_2O_8$ glass, the mean Al-O

88   coordination number (CN_{AlO}) reaches 5 and the elongation of Al-O bond length saturates around

89   10 GPa. In addition, it is probable that the permanent densification of aluminosilicate glass is

90   partially related to the irreversible increase in the CN_{AlO} (Lee et al. 2020). Thus, we are motivated

91   to determine the atomic structure of basaltic glass above 10 GPa and to compare the structures of

92   recovered glass from 6.0 GPa and above 10 GPa. X-ray and neutron diffraction give independent

93   structural information due to their different interaction to chemical species: neutron data is

94   weighted more heavily by O-O correlation, while X-ray data is weighted by Si-Si and O-O

95   correlation almost equally; thus, the comparison gives information on the partial structures.

96   Therefore, we have investigated the structure of basaltic glass at pressures of up to 12.3 and 18

97   GPa by XRD and ND, respectively. The structural change during decompression from 12.3 GPa

98   were also investigated by XRD.

99

4

100   EXPERIMENTAL METHODS

101   A basaltic glass was synthesized at ambient pressure by the same way as those described in

102   Ohashi et al. (2018). The chemical composition was $Si_{0.19}Al_{0.07}Fe_{0.03}Mg_{0.04}Ca_{0.05}Na_{0.02}O_{0.61}$. The

103   average number of non-bridging oxygen (NBO) per tetrahedrally coordinated cation (T), NBO/T,

104   of the glass was calculated to be 0.73 at ambient pressure from its chemical composition based on

105   the definition of Mysen et al. (1982).

106   In situ high-pressure XRD experiments were carried out in a pressure range from 7.3 GPa to

107   12.3 GPa using a cubic-type multi-anvil apparatus, MAX80 (e.g., Shimomura et al. 1984) at the

108   AR-NE5C beamline of the Photon Factory at KEK, Tsukuba, Japan. The data below 7.3 GPa are

109   taken in our previous study (Ohashi et al. 2018). The cell assembly used in the experiment is shown

110   in Figure 1. A boron-epoxy cube was used as a pressure-transmitting medium. In the hole drilled

111   at the center of the lower cube, a sintered MgO rod, a pressure marker, and sample are staked from

112   the bottom. For compression of the sample, we used the MA 6-6 (Nishiyama et al. 2008) consisting

113   of six tungsten carbide anvils with 4.0-mm truncated edge length. The generated pressures were

114   determined from the lattice parameter of NaCl mixed with MgO powder in the same weight ratio,

115   based on its Birch-Murnaghan equation of state, B-M EoS (Brown 1999).

116   In situ high-pressure ND experiments were carried out in a pressure range from 2 GPa to 18

117   GPa, using a VX4 Paris-Edinburgh press (Besson et al. 1992; Klotz et al. 2004) at the BL11

118   PLANET beamline (Hattori et al. 2015) of the Materials and Life Science Experimental Facility

119   (MLF) at J-PARC, Tokai, Japan. In the data collection at lower four pressures, the spheroidal

120   specimen with the size of ϕ6 mm × 3.6 mm was compressed with single toroidal anvils made of

121   tungsten carbide. In those at higher three pressures, the specimen with the size of ϕ4 mm × 3.1 mm

122   was compressed with double toroidal anvils made of sintered diamond. In both the experiments,

123   the specimen was contained in a gasket made of TiZr null alloy. The sample pressure was estimated

124   from the load applied to the anvils based on the pressure–load relationship determined beforehand.

5

125   In the XRD experiments, the diffraction profiles were collected at eight diffraction angles of

126      $2\theta = 4°, 6°, 8°, 11°, 14°, 17°, 21°$, and $25°$ by the energy-dispersive method in order to extend

127   accessible Q range. In the ND experiments, the diffraction data was collected at $2\theta \approx 90°$ by time-

128   of-flight method. For description of structure factors ($S^X(Q)$ for X-ray and $S^N(Q)$ for neutron), we

129   used the Faber-Ziman formalism which are expressed by:

$$S^X(Q) = \frac{I_{\mathrm{coh}}(Q)/N - \left\{\sum_i c_i \left[f_i(Q)\right]^2 - \left[\sum_i c_i f_i(Q)\right]^2\right\}}{\left[\sum_i c_i f_i(Q)\right]^2}, \tag{1a}$$

$$S^N(Q) = \frac{I_{\mathrm{coh}}(Q)/N - \left\{\sum_i c_i b_i^2 - [\sum_i c_i b_i]^2\right\}}{[\sum_i c_i b_i]^2}, \tag{1b}$$

130   where N, $I_{\mathrm{coh}}(Q)$, c_i, $f_i(Q)$, and b_i are the number of atoms, coherent scattering intensity, the

131   concentration, atomic scattering factor, and coherent scattering length of i atom, respectively. $S^X(Q)$

132   were obtained by correcting diffraction patterns by means of an MCEDX software (Funakoshi

133   1997) and $S^N(Q)$ by the nvaSq.py code developed at MLF. In the ND experiments, scattering

134   intensity of the sample were corrected using the data for compressed vanadium pellets and gaskets

135   recovered from high-pressure conditions. The detailed procedure is described in the reference

136   (Hattori et al. 2019).

137   The X-ray and neutron total pair distribution functions, $g^X(r)$, $g^N(r)$, are derived by Fourier

138   transformation of individual $S^{X,N}(Q)$ based on the following equation:

$$g^{X,N}(r) = 1 + \frac{1}{2\pi^2 nr} \int_{Q_{\min}}^{Q_{\max}} dQ\, Q[S^{X,N}(Q) - 1]M(Q)\sin(Qr), \tag{2}$$

139   where r is radial distance, n denotes the number density, and $M(Q)$ is a Lorch modification function

140   introduced to suppress the termination ripples of $g(r)$ (Lorch 1969). The number density used in

141   the analysis is listed in Table 2, which are calculated from the B-M EoS determined using the

142   densities measured by X-ray absorption method up to 9.1 GPa (Sakamaki, personal

143 communication). In the determination of the EoS, we used the EoSFit7-GUI software (Angel et al.

144 2014; Gonzalez-Platas et al. 2016). Here, the number density at ambient pressure is $n = 0.0722(5)$

145 Å^{-3} determined by Archimedes' method and the bulk modulus is $K_0 = 25(1)$ GPa with $K' = 4$

146 determined by X-ray absorption method (Sakamaki, personal communication). The average

147 distance of each pair correlation was derived by fitting total correlation function, $T(r) = 4\pi n r g(r)$,

148 with a sum of Gaussian functions (Figs. S1a, S1b, and S1c). After assigning each Gaussian function

149 to i-j atomic pair correlation, the average numbers of j atoms around i atoms (CN_{ij}^X for X-ray and

150 CN_{ij}^N for neutron) were calculated by integral of the Gaussian function fitted to each peak of $T^{X,N}(r)$

151 (Figs. S1a, S1b, and S1c) and $T_{ij}^X(r)$ (Figs. S1d and S1e) based on the following equations:

$$CN_{ij}^X = \frac{\left[\sum_i c_i f_i(0)\right]^2 c_j}{(2 - \delta_{ij})c_i c_j f_i(0) f_j(0)} \int_{r_{min}}^{r_{max}} dr \frac{A_{ij}}{\sigma_{ij}} \sqrt{\frac{2}{\pi}} e^{-2\left(\frac{r-r_{ij}}{\sigma_{ij}}\right)^2} r =$$

$$\frac{c_j}{w_{ij}^X(0)} \int_{r_{min}}^{r_{max}} dr \frac{A_{ij}}{\sigma_{ij}} \sqrt{\frac{2}{\pi}} e^{-2\left(\frac{r-r_{ij}}{\sigma_{ij}}\right)^2} r, \tag{3a}$$

$$CN_{ij}^N = \frac{\left[\sum_i c_i b_i\right]^2 c_j}{(2 - \delta_{ij})c_i c_j b_i b_j} \int_{r_{min}}^{r_{max}} dr \frac{A_{ij}}{\sigma_{ij}} \sqrt{\frac{2}{\pi}} e^{-2\left(\frac{r-r_{ij}}{\sigma_{ij}}\right)^2} r = \frac{c_j}{w_{ij}^N} \int_{r_{min}}^{r_{max}} dr \frac{A_{ij}}{\sigma_{ij}} \sqrt{\frac{2}{\pi}} e^{-2\left(\frac{r-r_{ij}}{\sigma_{ij}}\right)^2} r. \tag{3b}$$

152 Here, δ_{ij} is the Kronecker delta. A_{ij}, σ_{ij} and r_{ij} are the area, the full width at half maximum (FWHM),

153 and the center position of each Gaussian peak, respectively. The $w_{ij}^{X,N}$ is the X-ray/neutron

154 weighting factor for the i-j pairs (Table 1). Considering the Q dependence of $f_i(Q)$, the pseudo-

155 partial $g_{ij}^X(r)$ functions were also calculated based on the method of Prescher et al. (2017).

156

157 **RESULTS AND DISCUSSION**

158 **Structure factor**

159 Figure 2 shows $S^X(Q)$ and $S^N(Q)$ obtained in this study. Here, $S^X(Q)$ below 7 GPa are obtained

160 by reanalyzing the data taken in our previous study (Ohashi et al. 2018). The pressure dependences

161   of positions and FWHMs of the FSDP and PP are summarized in Figure 3 and Table 2. The peak

162   parameters were determined by decomposing each $S(Q)$ into a sum of Lorentzian functions. The

163   most pronounced changes were observed in the Q region below 10 Å^{-1}. At ambient pressure, the

164   FSDP position (Q_1) of $S^X(Q)$ is about 0.15 Å^{-1} higher than that of β-PST9 natural basalt glass

165   (Drewitt et al. 2013, XRD) with NBO/T of 0.84 (Ti and P are not considered). This difference in

166   Q_1 is attributed to the difference in their chemical compositions (NBO/T) and possibly P-T and

167   other physicochemical conditions where the natural melt vitrified. The FSDP at 2.2–2.3 Å^{-1} in

168    $S^X(Q)$ and $S^N(Q)$ shift toward a higher Q value linearly with pressure (Fig. 3a). In $S^N(Q)$, the FSDP

169   diminishes its intensity with increasing pressure. Based on the previously proposed interpretations

170   (Price et al. 1988; Elliott 1991; Wright 1994; Mei et al. 2008), the shift indicates a shrinkage in an

171   interval between -Si(Al)-O-Si(Al)- tetrahedral chains. According to a recent computational study

172   (Shi and Tanaka 2019), the FSDP mainly stems from a length scale related to the height of Si$_4$ or

173   Al$_4$ tetrahedron formed by four Si or Al cations adjacent to a Si(Al)O$_4$ tetrahedron. Therefore, the

174   shift of the FSDP may be interpreted by a pressure-induced contraction of Si$_4$ or Al$_4$ tetrahedra. It

175   is expected that the FSDP is largely contributed from a peak at ~2 Å^{-1} of the partial $S_{SiSi}(Q)$

176   (Adjaoud et al. 2008; Guignard and Cormier 2008; Shi and Tanaka 2019). The PP in $S^X(Q)$ around

177   3.1 Å^{-1} which is less prominent in the pressure range up to 4.7 GPa becomes discernable as a peak

178   above 4.7 GPa (see the inset in Fig. 2a). On the other hand, the PP in $S^N(Q)$ is prominent over entire

179   pressure range investigated and its height increases with pressure (Figs. 2a and 2b). The outstanding

180   PP in $S^N(Q)$ is expected to mainly come from a positive peak at ~3 Å^{-1} in the weighted partial w_{OO}^N

181    $\cdot S_{OO}(Q)$ (Adjaoud et al. 2008; Murakami et al. 2019; Onodera et al. 2020). The position of the PP

182   in $S^X(Q)$ shifts to lower Q values by compression to approximately 6.0 GPa, then it remains to be

183   3.1 Å^{-1} up to 11.3 GPa. On further compression, the PP slightly shifts to a higher Q value. In

184   contrast, the PP in $S^N(Q)$ shifts toward higher Q values up to 9 GPa, and to higher Q values more

185   sharply above 9 GPa. The intensification and the positional shift of the PP are attributed to the

186   structural change from an open structure to a densely packed one accompanied by increase in

187   packing fraction of oxygen atoms (Zeidler et al. 2014a; Salmon et al. 2016) and decrease in NBO

188   population (Ghosh et al. 2014; Ghosh and Karki 2018). This view is also consistent with that of

189   Guthrie et al. (2004), who argued that the pressure-induced collapse of the IRO largely originates

190   from changes in the O-O correlations. Here, the PP may be largely contributed from the second

191   peak in $S_{OO}(Q)$ as is the case for $CaAl_2Si_2O_8$ (Drewitt et al. 2015) and SiO_2 (Murakami et al. 2019;

192   Onodera et al. 2020) glasses. The ERO, which is strongly contributed from the PP, relates to a

193   propagation of the short-range order structure (Salmon et al. 2005). Hence, the sharper shift of the

194   PP above 9 GPa is considered to be attributed to the decrease in r_{OO}. In addition, the sharper shift

195   of the PP may also be due to the increase in CN_{AlO} which makes packing of oxygen atoms more

196   efficient. Additionally, the O-O distance (r_{OO}) starts to decrease and increase of CN_{OO} saturates at

197   8.5 at 9–13 GPa (Fig. 5). It is thereby considered that these changes reflect stable limits of the open

198   glass structure and the start of the decrease in NBO population. Based on the conception by Shi

199   and Tanaka (2019), the PP is primarily comprised of the edge length of a Si_4 or an Al_4 tetrahedron

200   and the height of a $Si(Al)O_4$ tetrahedron. Hence, the apparently different the PP position (Q_2) at

201   high pressures between $S^X(Q)$ and $S^N(Q)$ may come from the different contribution of the above

202   components due to the different weight of the scattering factors between X-ray and neutrons (Table

203   1), and/or the poor peak separation of the much smaller PP in $S^X(Q)$.

204   The FWHM of the FSDP in $S^N(Q)$, ΔQ_1, is invariant near 0.8 Å^{-1} up to 7–9 GPa, and then starts

205   to decrease (Fig. 3c). This decrease suggests the increase of the range of the IRO originating from

206   the FSDP ($\approx 2\pi/\Delta Q_1$) (Susman et al. 1988; Sokolov et al. 1992; Salmon 1994). The range of the

207   IRO is ~8 Å up to 7–9 GPa. It starts to increase above 7–9 GPa and reaches ~20 Å at 18 GPa. The

208   pressure-induced sharpening of the FSDP has been also observed in previous ND results for

209     $MgSiO_3$ and $CaSiO_3$ glasses (Salmon et al. 2019), and XRD and MD results for $CaAl_2Si_2O_8$ melt

210   and glass (Drewitt et al. 2015). On the other hand, as also reported by a previous ND study (Zeidler

211 et al. 2014a), the FSDP broadens by compression in the case of SiO_2 glass. The constant ΔQ_1 values

212 in modified glasses can be caused by the presence of modifier cations, which decreases the cavity

213 volume within the -Si(Al)-O-Si(Al)- network (Kohara et al. 2011; Onodera et al. 2019, 2020). The

214 contrasting pressure dependences of ΔQ_1 between modified and silica glasses may originate from

215 the difference in their typical ring sizes. For example, the most abundant -Si(Al)-O-Si(Al)- and -

216 Si(Mg)-O-Si(Mg)- ring sizes of $CaAl_2Si_2O_8$ melt (de Koker 2010) and MgO-SiO_2 glasses (Kohara

217 et al. 2011), respectively, range from 3- to 4-membered ones at ambient pressure. In the case of

218 SiO_2 glass, however, the 6-membered -Si-O-Si- ring is the most frequent (e.g., Galeener 1979;

219 Hemley et al. 1986; Kohara and Suzuya 2005). According to Wilding et al. (2012),

220 $(MgO)_{0.62}(SiO_2)_{0.38}$ glass (NBO/Si = 3.3) transforms into a more 'void-free and topologically

221 ordered' structure by compression. If this is also the case for other modified silicate glasses, the

222 increase in the IRO range will be manifested by this compression-induced topological ordering.

223 The monotonic decrease in the IRO range of SiO_2 glass is attributed to a gradual transition from

224 locally favored tetrahedral structure to disordered normal-liquid structure (Shi and Tanaka 2019;

225 Onodera et al. 2020). The FSDP of $S^x(Q)$ also tends to sharpen with increasing pressure (Fig. S2a).

226 On decompression the X-ray ΔQ_1 seems to change reversibly, and the X-ray ΔQ_1 of the glasses

227 recovered to 1 atm are almost the same as that of the uncompressed glass. This result implies that

228 the 'void-free and topologically ordered' structure under high pressure is not recoverable to

229 ambient.

230 As seen in Figure 3d, the FWHM of the PP (ΔQ_2) also represents different pressure

231 dependences between modified and unmodified glasses. The ΔQ_2 value for basaltic glass is almost

232 unchanged around 0.6 Å^{-1} up to ~18 GPa. The ΔQ_2 data for $MgSiO_3$ and $CaSiO_3$ glasses (Salmon

233 et al. 2019) represent similar behaviors. Hence, the range of the ERO is expected to be constant

234 around 10 Å up to ~18 GPa in the case of modified silicate glasses. ΔQ_2 for SiO_2 glass

235 monotonically decreases with pressure, suggesting steady increases in the range of the ERO

236 originating from PP and the packing of oxygen atoms. The cavity volume is smaller in modified

237 glass (Kohara et al. 2011; Wilding et al. 2012; Onodera et al. 2019, 2020). Hence, the ERO range

238 (Fig. 3d) and the packing of oxygen atoms (Fig. 7) of modified glasses at 1 atm are larger than

239 those of SiO_2 glass, which has a larger cavity volume than those of modified glasses at 1 atm

240 (Kohara et al. 2011). Contrastively, the dominant pressure-induced structural change of SiO_2 glass

241 is characterized by diminutions of the larger void volume and the larger ring size in conjunction

242 with the CN_{SiO} increase (Zeidler et al. 2014a). Unlike the case of the neutron ΔQ_2, the X-ray ΔQ_2

243 represents the non-linear pressure dependence on compression (Fig. S2b). The X-ray ΔQ_2 of the

244 recovered glasses are markedly broadened as the applied highest pressure increases. ΔQ_2 broadens

245 up to ambient pressure during decompression from 12.3 GPa. These scattered data probably come

246 from the small oscillation of the weighted partial $w_{OO}^X(Q) \cdot S_{OO}(Q)$ (Table 1); thus, the X-ray ΔQ_2

247 does not necessarily manifest the ERO range.

248 The third, fourth, and fifth peaks, respectively, at 4.5 Å^{-1}, 6–7 Å^{-1}, 8.5 Å^{-1} in $S^X(Q)$ reduce

249 their intensities and shift to higher Q values by compression (Fig. 2a). In $S^N(Q)$, the third peak at 5

250 Å^{-1} exhibits a slight reduction in intensity with pressure (Fig. 2b). Such weakening and shifting of

251 peaks are considered to reflect the gradual disordering and contraction of the short-range order

252 structure by pressurization, respectively. $S^X(Q)$ above ~10 Å^{-1} and $S^N(Q)$ above ~7 Å^{-1} show almost

253 identical oscillations.

254

255 **Pair distribution function**

256 The $g^X(r)$ and $g^N(r)$ functions under compression are depicted in Figures 4a and 4b,

257 respectively. The peaks in the r region above 1.4 Å can be assigned to correlations for Si(Al)-O

258 (1.6–1.7 Å), O-O (2.6–2.7 Å), Si(Al)-Si(Al) (3.1 Å), and M-Si(Al or M) (~3.2 Å) where M stands

259 for network modifying metal cations (= Fe^{2+}, Mg, Ca, and Na). In natural tholeiites with NBO/T of

260 0.7–0.8, Mg^{2+} and Fe^{2+} cations always function as network modifiers at ambient pressure, whereas

11

261   Na$^+$ cation as a charge compensator (Mysen and Richet 2018). Mysen and Richet (2018) further

262   reported that about 30–50% of Ca^{2+} cations work as network modifiers, while the others work as

263   charge compensators.

264   Figures 5a and 5b show changes of r_{ij} and CN_{ij} for Si(Al)-O and O-O pairs as a function of

265   pressure, respectively (the $CN_{\text{Si(Al)O}}$ data in the Fig. 5b and Table 3 are derived according to Eq.

266   3a). For the O-O correlation, the prominent peak at 2.6–2.7 Å in $g^N(r)$ is regarded as the

267   contribution only from the correlation between oxygens in SiO$_4$ tetrahedra (Fig. 4b). Here, it is

268   reported for SiO$_2$ glass that pressure dependence of Q_1 are similar to that of pressure dependence

269   of the number density (Wakabayashi et al. 2011; Zanatta et al. 2014). Based on this relation, the

270   number density of recovered glass was indirectly estimated from Q_1 during decompression from

271   the pressure dependence of Q_1 during compression. Firstly, virtual pressures P_{decomp} were calculated

272   by substituting Q_1 of the decompressed glass for a linear function obtained from the linear fitting

273   of the pressure-Q_1 relation on compression. n on decompression were then estimated by

274   substituting the calculated pressures P_{decomp} for the B-M EoS on compression. The $r_{\text{Si(Al)O}}$ and

275    $CN_{\text{Si(Al)O}}$ remain approximately invariant at $r_{\text{Si(Al)O}} = 1.62$–$1.64$ Å and $CN_{\text{Si(Al)O}} = 4$ up to 10.3 GPa,

276   respectively. However, $CN_{\text{Si(Al)O}}$ at pressures higher than 10.3 GPa represents lower values of about

277   3. It is probable that the lowering results from the separation of Si-O and Al-O correlations due to

278   preferential increase in CN_{AlO} with pressure accompanied by the increase in r_{AlO}. When only w_{SiO}^N

279   is used instead of $w_{\text{Si(Al)O}}^N = w_{\text{SiO}}^N + w_{\text{AlO}}^N$ in Eq. 3b, provided that the first peak of $g(r)$ is

280   contributed only from the Si-O correlation, $CN_{\text{Si(Al)O}}$ is derived as 4 at these pressures (see footnote

281   b in Table 3). Additionally, the mean O-Si(Al)-O intra-tetrahedral angle, $\Theta_{\text{OSi(Al)O}}$ (=

282    $2\sin^{-1}[r_{\text{OO}}/(2r_{\text{Si(Al)O}})]$), decreases from 108°–110° to 105° above 13 GPa (Fig. 5c and Table 3),

283   suggesting the deformation of Si(Al)O$_4$ polyhedra. Considering the previously reported $\Theta_{\text{OSi(Al)O}}$

284   distribution and CN_{AlO} data of CaAl$_2$Si$_2$O$_8$ glass (Ghosh and Karki 2018) and basaltic melt

285   (Majumdar et al. 2020), the decrease in $\Theta_{\text{OSi(Al)O}}$ also suggests a preferential increase in CN_{AlO}

286   above 5 at 13–18 GPa. As expected, the Q dependence of $f_i(Q)$ significantly influences the $CN_{\mathrm{Si(Al)O}}^{\mathrm{X}}$

287   values (Fig. S3, and Tables 3 and S1). A possible source of the difference is the lower amplitude

288   of $c_{\mathrm{O}}\{1/w_{\mathrm{Si(Al)O}}^{\mathrm{X}}(0) - 1 + F[w_{\mathrm{Si(Al)O}}^{\mathrm{X}}(Q)]\}$ than that of $[c_{\mathrm{O}}/w_{\mathrm{Si(Al)O}}^{\mathrm{X}}(0)]F[w_{\mathrm{Si(Al)O}}^{\mathrm{X}}(0)]$ (cf. "CN

289   Estimation" section in Prescher et al. (2017) and Eq. 3a in this study, respectively). Here, $w_{\mathrm{Si(Al)O}}^{\mathrm{X}}(0)$

290   = 3.4141 (Table 1) for various Q ranges, and $F[\cdot]$ denotes the Fourier transform, which is the same

291   form as Eq. 2 ($M(Q)$ is not applied). The pressure-dependent difference in the $CN_{\mathrm{Si(Al)O}}$ values from

292   two methods may be attributed to the possibility that the difference between r_{SiO} and r_{AlO} changes

293   with pressure. A superposition of the Si(Al)-Si(Al), M-Si(Al or M), and O-O correlations are

294   observed in $g^{\mathrm{X}}(r)$ in the region from 2.5 Å to 3.5 Å. These correlations tend to weaken and shift

295   toward lower r value with pressure up to 9.0 GPa and subsequently shows a hump around 2.7 Å

296   (Fig. 4a). There should be many types of correlation in the region from 2.5 Å to 3.5 Å. Hence, a

297   precise determination of each correlation remains to be confirmed. Nevertheless, the Si(Al)-Si(Al)

298   peak generally shifts toward a lower r value and reduce its intensity by compression. These shifting

299   and reduction in intensity infer the decrease and diversification of the Si(Al)-O-Si(Al) angle,

300   respectively, as indicated by previous MD studies on silicate glasses (Shimoda and Okuno 2006;

301   Ghosh et al. 2014; Ghosh and Karki 2018). According to the pressure evolution of the partial $g_{\mathrm{MSi}}(r)$

302   in MgSiO$_3$ and CaSiO$_3$ (Shimoda and Okuno 2006) glasses, the M-Si correlation is represented by

303   a sum of two components with individual characteristic lengths: correlations in edge- and corner-

304   shared polyhedra formed by MO$_x$ (x: integer) and Si(Al)O$_4$ polyhedra, where the latter becomes

305   more abundant at high pressures. Therefore, the broadening and splitting of the peaks in $g^{\mathrm{X}}(r)$ in

306   the region from 2.5 Å to 3.5 Å can be attributed to the increase in the number of edge-sharing

307   polyhedral pairs compared to the corner-sharing pairs.

308   As pictured in Figure 5a, r_{OO} remains constant at 2.64–2.66 Å up to 9 GPa, then starts to

309   decrease toward 2.60 Å at 18 GPa. This decrease may be due to the polyhedral deformation as

310   indicated by the acute decrease in $\Theta_{\mathrm{OSi(Al)O}}$ (Fig. 5c). CN_{OO} starts to increase from 4.5 at 2–4 GPa

311   and the increase is saturated around 8.5 at pressures above 9–13 GPa (Fig. 5b). These pressure

312   dependences can be interpreted by the mechanism that the volume contraction cannot occur any

313   longer by bending tetrahedral networks. This is consistent with the observation that $CN_{\mathrm{Si(Al)O}}$

314   increases above 9–13 GPa (Fig. 5b), which is consistent with a view that additional oxygen atoms

315   pushed into $\mathrm{Si(Al)O_4}$ tetrahedra by compression (Guthrie et al. 2004; Salmon 2018). The larger

316   errors of r_{OO} and CN_{OO} at higher pressures are due to the worse separation of this peak from the

317   shoulder at approximately 2.9 Å. Assuming the ideal tetrahedral geometry, previously determined

318    $\mathrm{AlO_5}$ geometries of molten $\mathrm{Al_2O_3}$ (Skinner et al. 2013), and r_{AlO} of $\mathrm{CaAl_2O_4}$ glass under pressure

319   (Drewitt et al. 2015), r_{OO} at 7–18 GPa are expected at 2.97–3.09 Å in the case of the $\mathrm{AlO_4}$

320   tetrahedron, and at 2.85–2.96 Å in the case of $\mathrm{AlO_5}$ square pyramid and trigonal bipyramid. The

321   O-O correlations in MO_x polyhedra are expected around 3 Å (e.g., Weigel et al. 2008). Hence, this

322   shoulder can be assigned to the O-O correlation either in $\mathrm{AlO_4}$, $\mathrm{AlO_5}$, or MO_x polyhedra. According

323   to a previous classical MD study on $\mathrm{CaAl_2Si_2O_8}$ melt by Spera et al. (2009), many of $\mathrm{Si(Al)O_5}$

324   polyhedra exist as trigonal bipyramids, which may be abundant in basaltic glass as well.

325

326   **Structural change on decompression**

327   Figure 6a compares the $S^{\mathrm{X}}(Q)$ of uncompressed basaltic glass with those of basaltic glass

328   during decompression from 6.0 GPa (Ohashi et al. 2018) and 12.3 GPa. Some notable changes are

329   observed in the FSDP, PP, and peaks at 6–7 $\mathrm{Å^{-1}}$ (the inset in Figure 6a). On decompression from

330   12.3 GPa, Q_1 shifts to lower Q values and reaches 2.11 $\mathrm{Å^{-1}}$ at 1 atm, which is 0.09 $\mathrm{Å^{-1}}$ larger than

331   that of the glass recovered from 6.0 GPa (Figure 3a and Table 2). Although Q_1 of the glass

332   recovered from 6.0 GPa is larger than that of the uncompressed glass, the difference is smaller than

333   the difference between our basaltic glass and the natural basalt glass used in Drewitt et al. (2013).

334   Hence, the recovered glass might not be irreversibly densified yet. The amount of the shift in Q_1

335   during the decompression from 12.3 GPa is smaller than that for normal glass during compression.

336   During decompression, the PP diminishes and Q_2 follows the pressure dependence on compression.

337   The peak at 6–7 Å^{-1} diminishes and shifts to lower Q values with decreasing pressure from 12.3

338   GPa, whereas the Q value of that peak of the glass recovered from 6.0 GPa is almost the same as

339   the ambient-pressure value of ordinary glass. This also reflects the structural differences between

340   fully and non-fully densified glasses.

341   Figure 6b shows a comparison of $g^X(r)$ during the compression and decompression. In the glass

342   recovered from 12.3 GPa to ambient pressure, the peak around 3 Å, which is assigned to the

343   superposition of the Si(Al or M)-Si(Al or M) correlation, are weak and split. The shape of the peak

344   is different from those of ordinary glass and the glass recovered from 6.0 GPa to ambient pressure.

345   This suggests that the Si(Al or M)-Si(Al or M) angle remains smaller than that of uncompressed

346   glass and some of the connections of edge-shared polyhedra are retained after the release of

347   pressure. As illustrated in Figure 5a, the $r_{Si(Al)O}$ of the glass recovered from 12.3 GPa (1.67 Å) is

348   larger than that of the ordinary glass and the glass recovered from 6.0 GPa (1.65 Å). The $CN_{Si(Al)O}$

349   of both the recovered glasses are calculated at approximately 5, which is slightly higher than that

350   of the ordinary glass. This result can support the above-mentioned idea that the onset of permanent

351   densification is related to the preferential increase in CN_{AlO}.

352

353   **IMPLICATIONS**

354   Since basalt is the typical composition of magmas produced in the Earth, the properties of

355   basaltic glasses have been investigated as proxies for deep magmas (Kono et al. 2008; Liu and Lin

356   2014; Clark et al. 2016). One of the notable observations in the present work is the rise of CN_{OO} at

357   2–4 GPa (Fig. 5b). According to a previous high-pressure Brillouin scattering experiment (Liu and

358   Lin 2014), an Icelandic basalt glass (NBO/T = 0.8) exhibits anomalies (kinks) in the pressure

359   dependence of P- and S-wave velocities around 2 GPa. Such velocity anomalies have been

360   observed for many other kinds of silicate glasses (e.g., Sakamaki 2018; Moulton et al. 2019). It has

361   been interpreted that these anomalies are associated with an elastic softening caused by pressure-

362   induced diminutions of the Si(Al)-O-Si(Al) angle and the inter-polyhedral void (e.g., Liu and Lin

363   2014; Sakamaki et al. 2014). In the case of basaltic glass, the anomalous pressure dependence of

364   acoustic wave velocities takes place at pressures where CN_{OO} starts to increase. Oxygen is the

365   largest ion, and its concentration is the highest in basaltic glass. Hence, the cavity volume is thought

366   to be largely controlled by the partial ionic volume of oxygen, $(4/3)\pi r_O^3 nc_O$ (Fig. S4). Here, r_O (=

367    $r_{OO}/2$) is the mean ionic radius of oxygen ion. It is thereby expected that CN_{OO} starts to increase

368   when the inter-tetrahedral voids and the packing fraction of O ions reach certain values on

369   compression. Thus, the saturation of elastic softening near 2 GPa can be reflected by the onset of

370   CN_{OO} increase. Furthermore, the onset of CN_{OO} increase could signal the anomaly in elastic moduli

371   of silicate glasses.

372   The present ND experiments also demonstrate a possibility that CN_{AlO} starts to increase around

373   10 GPa. The increase in $CN_{Si(Al)O}$ is expected to largely correlated to the viscosity of basaltic melt,

374   according to previous experimental (e.g., Poe et al. 1997; Sakamaki et al. 2013) and ab initio MD

375   (Majumdar et al. 2020) studies. Majumdar et al. (2020) have predicted that the $CN_{Si(Al)O}$ increase,

376   particularly the emergence of sixfold coordinated species, causes the steady increase in the

377   viscosity of basaltic melt at 18–50 GPa. In addition, the density of MORB melt becomes closer to

378   that of the surrounding mantle solid at higher pressure (Sakamaki et al. 2006; Sanloup et al. 2013;

379   Bajgain et al. 2015). These earlier results suggest that the MORB melt is more immobile and likely

380   to stabilize at deeper Earth, especially above the 410-km discontinuity and beneath the 660-km

381   discontinuity.

382   As proposed and disputed in recent studies (Wang et al. 2014; Zeidler et al. 2014b; Kono et al.

383   2016, 2020; Du and Tse 2017; Prescher et al. 2017; Murakami et al. 2019), oxygen packing fraction

384   (η_O) can be a good measure to describe high-pressure structural changes of network-forming oxide

385   liquids and glasses. However, as pointed out by previous ab initio MD (Du and Tse 2017) and XRD

386 (Prescher et al. 2017) studies, there was a difficulty in estimating the ionic radius of oxygen under

387 pressure. This is because one must assume the specific and ideal $Si(Al)O_x$ coordination geometry

388 at given pressure. We calculated the η_O values using the experimentally obtained r_{OO} values. The

389 η_O were calculated based on the following definition of Zeidler et al. (2014b):

$$\eta_O = \frac{4}{3}\pi r_O^3 nc_O \Big/ \left[1 - \sum_M \frac{4}{3}\pi r_M^3 nc_M\right].$$

(4)

390 Here, r_M is the mean ionic radius of M ion. The r_M values are estimated from the computationally

391 obtained pressure-r_{MO} relationship at 0–70 GPa and 3000 K for the molten mid-oceanic ridge basalt,

392 MORB (Karki et al. 2018). The η_O values are listed in Table 3. Due to the small radii and the low

393 concentrations of Si, Al, and M cations compared to those of O anions in basaltic and silica glasses,

394 the η_O of these glasses can be treated as comparable values with the dense random packing of equal

395 hard spheres (Fig. S4). Although we can only do a rough estimation of the random-close packing

396 (RCP) limit of basaltic glass, the contribution of Si(Al) and M ions might be very small because

397 the partial ionic volume of Si(Al) plus M is about 10 times smaller than that of O ion (Fig. S5). As

398 pictured in Figure 7, η_O of basaltic and SiO_2 glasses exceed the RCP limit of equal hard spheres,

399 $\eta_{RCP} = 0.634$ (Song et al. 2008), around 10 GPa and 13 GPa, respectively. These excesses are

400 unphysical results, since the monodisperse hard-sphere glass cannot pack denser than the RCP

401 (e.g., Parisi and Zamponi 2010). Our ND experiments show that $CN_{OO} = 8.6$ at 13 GPa, which is

402 inconsistent with the mean coordination number in the RCP of equal spheres, $CN \approx 6$ (Nolan and

403 Kavanagh 1992; Silbert et al. 2002; Song et al. 2008). In addition, the Si-O covalent bond remains

404 around 10–13 GPa, and thus Si and O atoms have the angular correlation in the present pressure

405 condition. Therefore, η_O should be much lower than η_{RCP}. The overestimation of η_O is probably

406 attributed to the poor approximation of r_O. This is because r_{OO} is determined not only by r_O, but by

407 intra-polyhedral bond lengths and bond angles of $Si(Al)O_x$ and MO_x polyhedra. Hence,

408 approximating r_O as $r_{OO}/2$ is the overestimation. For these reasons, the packing limit of oxygen ions

17

409   cannot explain the high-pressure structural changes of silica and silicate glasses at the present

410   pressure condition. At the relatively low pressure region up to ~20 GPa, the Si(Al)-O bond is highly

411   covalent, and the O-Si(Al)-O angle has a sharper distribution (Majumdar et al. 2020). In this

412   pressure region, the inter- and intra-polyhedral bond angles, rather than the packing of atoms, are

413   considered to be essential values which characterize the structure of silica and silicate glasses.

414   Above ~20 GPa, the Si(Al)-O bond becomes more ionic and the O-Si(Al)-O angle distribution

415   significantly diversifies (Majumdar et al. 2020). In addition, SiO_2 glass has a close-packed structure

416   above ~30 GPa (Prescher et al. 2017; Murakami et al. 2019), implying that the packing of atoms

417   starts to have some contributions to the structural change. At 200 GPa, the O-Si-O angle

418   distribution of SiO_2 glass is highly analogous to that of the random-packing structure of hard

419   spheres (Murakami et al. 2019). Thus, on the basis of hard-sphere approximation, η_O could be a

420   powerful tool to quantitatively describe the structure of silica and silicate glasses/melts at multi-

421   megabar pressures.

422

18

434   beamline with the approval of the KEK (Proposal No. 2017G580). The ND experiments were

435   performed at BL11 PLANET beamline at the MLF of the J-PARC under user programs (Proposal

436   Nos. 2017A0012 and 2017B0061). The authors would like to thank Enago (www.engo.jp) for the

437   English language review. There are no conflicts of interest to declare. T.S. and A.S. designed this

438   work. T.O. wrote the paper with contributions from all co-authors. T.O., T.S., N.H., K.F., and A.S.

439   conducted the XRD experiments. T.O., T.S., T.H., and J.A. performed the ND experiments. T.O.

440   and T.S. analyzed the data with help from K.F. and T.H.

441

442   REFERENCES CITED

443   Adjaoud, O., Steinle-Neumann, G., and Jahn, S. (2008) Mg_2SiO_4 liquid under high pressure from

444   molecular dynamics. Chemical Geology, 256, 185–192.

445   Angel, R.J., Gonzalez-Platas, J., and Alvaro, M. (2014) EosFit7c and a Fortran module (library)

446   for equation of state calculations. Zeitschrift für Kristallographie, 229, 405–419.

447   Bajgain, S., Ghosh, D.B., and Karki, B.B. (2015) Structure and density of basaltic melts at mantle

448   conditions from first-principles simulations. Nature Communications, 6, 8578.

449   Benmore, C.J., Soignard, E., Amin, S.A., Guthrie, M., Shastri, S.D., Lee, P.L., and Yarger, J.L.

450   (2010) Structural and topological changes in silica glass at pressure. Physical Review B,

451   81, 054105.

452   Benmore, C.J., Soignard, E., Guthrie, M., Amin, S.A., Weber, J.K.R., McKiernan, K., Wilding,

453   M.C., and Yarger, J.L. (2011) High pressure x-ray diffraction measurements on Mg_2SiO_4

454   glass. Journal of Non-Crystalline Solids, 357, 2632–2636.

455   Besson, J.M., Nelmes, R.J., Hamel, G., Loveday, J.S., Weill, G., and Hull, S. (1992) Neutron

456   powder diffraction above 10 GPa. Physica B: Condensed Matter, 180–181, 907–910.

457   Brown, J.M. (1999) The NaCl pressure standard. Journal of Applied Physics, 86, 5801–5808.

458   Clark, A.N., Lesher, C.E., Jacobsen, S.D., and Wang, Y. (2016) Anomalous density and elastic

19

459   properties of basalt at high pressure: Reevaluating of the effect of melt fraction on seismic
460   velocity in the Earth's crust and upper mantle. Journal of Geophysical Research: Solid
461   Earth, 121, 4232–4248.

462 de Koker, N. (2010) Structure, thermodynamics, and diffusion in $CaAl_2Si_2O_8$ liquid from first-
463   principles molecular dynamics. Geochimica et Cosmochimica Acta, 74, 5657–5671.

464 Drewitt, J.W.E., Sanloup, C., Bytchkov, A., Brassamin, S., and Hennet, L. (2013) Structure of
465         $(Fe_xCa_{1-x}O)_y(SiO_2)_{1-y}$ liquids and glasses from high-energy x-ray diffraction: Implications
466   for the structure of natural basaltic magmas. Physical Review B, 87, 224201.

467 Drewitt, J.W.E., Jahn, S., Sanloup, C., de Grouchy, C., Garbarino, G., and Hennet, L. (2015)
468   Development of chemical and topological structure in aluminosilicate liquids and glasses
469   at high pressure. Journal of Physics: Condensed Matter, 27, 105103.

470 Du, X., and Tse, J.S. (2017) Oxygen packing fraction and the structure of silicon and germanium
471   oxide glasses. The Journal of Physical Chemistry B, 121, 10726–10732.

472 Elliott, S.R. (1991) Medium-range structural order in covalent amorphous solids. Nature, 354, 445.

473 Funakoshi, K. (1997) Energy-dispersive x-ray diffraction study for alkali silicate melts using
474   synchrotron radiation under high pressure and temperature. Ph. D. thesis, Tokyo Institute
475   of Technology, Meguro, Tokyo.

476 Galeener, F.L. (1979) Band limits and the vibrational spectra of tetrahedral glasses. Physical
477   Review B, 19, 4292–4297.

478 Ghosh, D.B., and Karki, B.B. (2018) First-principles molecular dynamics simulations of anorthite
479   ($CaAl_2Si_2O_8$) glass at high pressure. Physics and Chemistry of Minerals, 45, 575–587.

480 Ghosh, D.B., Karki, B.B., and Stixrude, L. (2014) First-principles molecular dynamics simulations
481   of $MgSiO_3$ glass: Structure, density, and elasticity at high pressure. American Mineralogist,
482   99, 1304–1314.

483 Gonzalez-Platas, J., Alvaro, M., Nestola, F., and Angel, R. (2016) *EosFit7-GUI*: a new graphical

484   user interface for equation of state calculations, analyses and teaching. Journal of Applied

485   Crystallography, 49, 1377–1382.

486   Grimsditch, M. (1984) Polymorphism in amorphous SiO_2. Physical Review Letters, 52, 2379–

487   2381.

488   Guignard, M., and Cormier, L. (2008) Environments of Mg and Al in MgO–Al_2O_3–SiO_2 glasses: A

489   study coupling neutron and X-ray diffraction and Reverse Monte Carlo modeling. Chemical

490   Geology, 256, 111–118.

491   Guthrie, M., Tulk, C.A., Benmore, C.J., Xu, J., Yarger, J.L., Klug, D.D., Tse, J.S., Mao, H., and

492   Hemley, R.J. (2004) Formation and structure of a dense octahedral glass. Physical Review

493   Letters, 93, 115502.

494   Hattori, T., Sano-Furukawa, A., Arima, H., Komatsu, K., Yamada, A., Inamura, Y., Nakatani, T.,

495   Seto, Y., Nagai, T., Utsumi, W., and others (2015) Design and performance of high-pressure

496   PLANET beamline at pulsed neutron source at J-PARC. Nuclear Instruments and Methods

497   in Physics Research Section A: Accelerators, Spectrometers, Detectors and Associated

498   Equipment, 780, 55–67.

499   Hattori, T., Sano-Furukawa, A., Machida, S., Abe, J., Funakoshi, K., Arima, H., and Okazaki, N.

500   (2019) Development of a technique for high pressure neutron diffraction at 40 GPa with a

501   Paris-Edinburgh press. High Pressure Research, 39, 417–425.

502   Hemley, R.J., Mao, H.K., Bell, P.M., and Mysen, B.O. (1986) Raman spectroscopy of SiO_2 glass

503   at high pressure. Physical Review Letters, 57, 747–750.

504   Karki, B.B., Ghosh, D.B., and Bajgain, S.K. (2018) Simulation of Silicate Melts Under Pressure.

505   In Y. Kono and C. Sanloup, Eds., Magmas Under Pressure: Advances in High-Pressure

506   Experiments on Structure and Properties of Melts pp. 419–453. Elsevier, Amsterdam.

507   Klotz, S., Hamel, G., and Frelat, J. (2004) A new type of compact large-capacity press for neutron

508   and x-ray scattering. High Pressure Research, 24, 219–223.

509   Kohara, S., and Suzuya, K. (2005) Intermediate-range order in vitreous SiO_2 and GeO_2. Journal of
510   Physics: Condensed Matter, 17, S77–S86.

511   Kohara, S., Akola, J., Morita, H., Suzuya, K., Weber, J.K.R., Wilding, M.C., and Benmore, C.J.
512   (2011) Relationship between topological order and glass forming ability in densely packed
513   enstatite and forsterite composition glasses. Proceedings of the National Academy of
514   Sciences, 108, 14780–14785.

515   Kono, Y., Ohfuji, H., Higo, Y., Yamada, A., Inoue, T., Irifune, T., and Funakoshi, K. (2008) Elastic
516   wave velocities and Raman shift of MORB glass at high pressures. Journal of Mineralogical
517   and Petrological Sciences, 103, 126–130.

518   Kono, Y., Kenney-Benson, C., Ikuta, D., Shibazaki, Y., Wang, Y., and Shen, G. (2016) Ultrahigh-
519   pressure polyamorphism in GeO_2 glass with coordination number >6. Proceedings of the
520   National Academy of Sciences, 113, 3436–3441.

521   Kono, Y., Shibazaki, Y., Kenney-Benson, C., Wang, Y., and Shen, G. (2018) Pressure-induced
522   structural change in $MgSiO_3$ glass at pressures near the Earth's core–mantle boundary.
523   Proceedings of the National Academy of Sciences, 115, 1742–1747.

524   Kono, Y., Shu, Y., Kenney-Benson, C., Wang, Y., and Shen, G. (2020) Structural evolution of SiO_2
525   glass with Si coordination number greater than 6. Physical Review Letters, 125, 205701.

526   Lee, S.K., Mun, K.Y., Kim, Y.-H., Lhee, J., Okuchi, T., and Lin, J.-F. (2020) Degree of permanent
527   densification in oxide glasses upon extreme compression up to 24 GPa at room temperature.
528   The Journal of Physical Chemistry Letters, 11, 2917–2924.

529   Liu, J., and Lin, J.-F. (2014) Abnormal acoustic wave velocities in basaltic and (Fe,Al)-bearing
530   silicate glasses at high pressures. Geophysical Research Letters, 41, 8832–8839.

531   Lorch, E. (1969) Neutron diffraction by germania, silica and radiation-damaged silica glasses.
532   Journal of Physics C: Solid State Physics, 2, 229–237.

533   Majumdar, A., Wu, M., Pan, Y., Iitaka, T., and Tse, J.S. (2020) Structural dynamics of basaltic melt

534   at mantle conditions with implications for magma oceans and superplumes. Nature
535   Communications, 11, 4815.

536 Meade, C., and Jeanloz, R. (1988) Effect of a coordination change on the strength of amorphous
537   SiO_2. Science, 241, 1072–1074.

538 Mei, Q., Benmore, C.J., Sen, S., Sharma, R., and Yarger, J.L. (2008) Intermediate range order in
539   vitreous silica from a partial structure factor analysis. Physical Review B, 78, 144204.

540 Moulton, B.J.A., Henderson, G.S., Martinet, C., Martinez, V., Sonneville, C., and de Ligny, D.
541   (2019) Structure—longitudinal sound velocity relationships in glassy anorthite
542   ($CaAl_2Si_2O_8$) up to 20 GPa: An *in situ* Raman and Brillouin spectroscopy study. Geochimica
543   et Cosmochimica Acta, 261, 132–144.

544 Murakami, M., Kohara, S., Kitamura, N., Akola, J., Inoue, H., Hirata, A., Hiraoka, Y., Onodera, Y.,
545   Obayashi, I., Kalikka, J., and others (2019) Ultrahigh-pressure form of SiO_2 glass with
546   dense pyrite-type crystalline homology. Physical Review B, 99, 045153.

547 Mysen, B.O., and Richet, P. (2018) Silicate Glasses and Melts, 2nd ed., 720 p. Elsevier Science,
548   Amsterdam.

549 Mysen, B.O., Virgo, D., and Seifert, F.A. (1982) The structure of silicate melts: Implications for
550   chemical and physical properties of natural magma. Reviews of Geophysics, 20, 353.

551 Nishiyama, N., Wang, Y., Sanehira, T., Irifune, T., and Rivers, M. (2008) Development of the Multi-
552   anvil Assembly 6-6 for DIA and D-DIA type high-pressure apparatuses. High Pressure
553   Research, 28, 307–314.

554 Nolan, G.T., and Kavanagh, P.E. (1992) Computer simulation of random packing of hard spheres.
555   Powder Technology, 72, 149–155.

556 Ohashi, T., Sakamaki, T., Funakoshi, K., and Suzuki, A. (2018) Pressure–induced structural
557   changes of basaltic glass. Journal of Mineralogical and Petrological Sciences, 113, 286–
558   292.

559   Onodera, Y., Takimoto, Y., Hijiya, H., Taniguchi, T., Urata, S., Inaba, S., Fujita, S., Obayashi, I.,
560   Hiraoka, Y., and Kohara, S. (2019) Origin of the mixed alkali effect in silicate glass. NPG
561   Asia Materials, 11, 1–11.

562   Onodera, Y., Kohara, S., Salmon, P.S., Hirata, A., Nishiyama, N., Kitani, S., Zeidler, A., Shiga, M.,
563   Masuno, A., Inoue, H., and others (2020) Structure and properties of densified silica glass:
564   characterizing the order within disorder. NPG Asia Materials, 12, 1–16.

565   Parisi, G., and Zamponi, F. (2010) Mean-field theory of hard sphere glasses and jamming. Reviews
566   of Modern Physics, 82, 789–845.

567   Park, S.Y., and Lee, S.K. (2018) Probing the structure of Fe-free model basaltic glasses: A view
568   from a solid-state ^{27}Al and ^{17}O NMR study of Na-Mg silicate glasses, Na_2O-MgO-Al_2O_3-
569   SiO_2 glasses, and synthetic Fe-free KLB-1 basaltic glasses. Geochimica et Cosmochimica
570   Acta, 238, 563–579.

571   Petitgirard, S., Sahle, C.J., Weis, C., Gilmore, K., Spiekermann, G., Tse, J.S., Wilke, M., Cavallari,
572   C., Cerantola, V., and Sternemann, C. (2019) Magma properties at deep Earth's conditions
573   from electronic structure of silica. Geochemical Perspectives Letters, 32–37.

574   Poe, B.T., McMillan, P.F., Rubie, D.C., Chakraborty, S., Yarger, J., and Diefenbacher, J. (1997)
575   Silicon and oxygen self-diffusivities in silicate liquids measured to 15 gigapascals and 2800
576   kelvin. Science, 276, 1245–1248.

577   Prescher, C., Prakapenka, V.B., Stefanski, J., Jahn, S., Skinner, L.B., and Wang, Y. (2017) Beyond
578   sixfold coordinated Si in SiO_2 glass at ultrahigh pressures. Proceedings of the National
579   Academy of Sciences, 114, 10041–10046.

580   Price, D.L., Moss, S.C., Reijers, R., Saboungi, M.-L., and Susman, S. (1988) Intermediate-range
581   order in glasses and liquids. Journal of Physics C: Solid State Physics, 21, L1069–L1072.

582   Price, D.L., Ellison, A.J.G., Saboungi, M.-L., Hu, R.-Z., Egami, T., and Howells, W.S. (1997)
583   Short-, intermediate-, and extended-range order in rubidium germanate glasses. Physical
584   Review B, 55, 11249–11255.

585   Ryuo, E., Wakabayashi, D., Koura, A., and Shimojo, F. (2017) *Ab initio* simulation of permanent
586   densification in silica glass. Physical Review B, 96, 054206.

587   Sakamaki, T. (2018) Structure and Properties of Silicate Magmas. In Y. Kono and C. Sanloup, Eds.,
588   Magmas Under Pressure: Advances in High-Pressure Experiments on Structure and
589   Properties of Melts pp. 323–341. Elsevier, Amsterdam.

590   Sakamaki, T., Suzuki, A., and Ohtani, E. (2006) Stability of hydrous melt at the base of the Earth's
591   upper mantle. Nature, 439, 192–194.

592   Sakamaki, T., Suzuki, A., Ohtani, E., Terasaki, H., Urakawa, S., Katayama, Y., Funakoshi, K.,
593   Wang, Y., Hernlund, J.W., and Ballmer, M.D. (2013) Ponded melt at the boundary between
594   the lithosphere and asthenosphere. Nature Geoscience, 6, 1041–1044.

595   Sakamaki, T., Kono, Y., Wang, Y., Park, C., Yu, T., Jing, Z., and Shen, G. (2014) Contrasting sound
596   velocity and intermediate-range structural order between polymerized and depolymerized
597   silicate glasses under pressure. Earth and Planetary Science Letters, 391, 288–295.

598   Salmon, P.S. (1994) Real space manifestation of the first sharp diffraction peak in the structure
599   factor of liquid and glassy materials. Proceedings of the Royal Society A: Mathematical,
600   Physical and Engineering Sciences, 445, 351–365.

601   Salmon, P.S. (2018) Densification Mechanisms of Oxide Glasses and Melts. In Y. Kono and C.
602   Sanloup, Eds., Magmas Under Pressure: Advances in High-Pressure Experiments on
603   Structure and Properties of Melts pp. 343–369. Elsevier, Amsterdam.

604   Salmon, P.S., Martin, R.A., Mason, P.E., and Cuello, G.J. (2005) Topological versus chemical
605   ordering in network glasses at intermediate and extended length scales. Nature, 435, 75–
606   78.

607   Salmon, P.S., Barnes, A.C., Martin, R.A., and Cuello, G.J. (2006) Glass fragility and atomic
608   ordering on the intermediate and extended range. Physical Review Letters, 96, 235502.

609   Salmon, P.S., Drewitt, J.W.E., and Zeidler, A. (2016) Neutron diffraction as a probe of liquid and

610   glass structures under extreme conditions. Neutron News, 27, 22–26.

611   Salmon, P.S., Moody, G.S., Ishii, Y., Pizzey, K.J., Polidori, A., Salanne, M., Zeidler, A., Buscemi,
612   M., Fischer, H.E., Bull, C.L., and others (2019) Pressure induced structural transformations
613   in amorphous $MgSiO_3$ and $CaSiO_3$. Journal of Non-Crystalline Solids: X, 3, 100024.

614   Sanloup, C. (2016) Density of magmas at depth. Chemical Geology, 429, 51–59.

615   Sanloup, C., Drewitt, J.W.E., Konôpková, Z., Dalladay-Simpson, P., Morton, D.M., Rai, N., van
616   Westrenen, W., and Morgenroth, W. (2013) Structural change in molten basalt at deep
617   mantle conditions. Nature, 503, 104–107.

618   Sato, T., and Funamori, N. (2008) Sixfold-coordinated amorphous polymorph of SiO_2 under high
619   pressure. Physical Review Letters, 101, 255502.

620   ——— (2010) High-pressure structural transformation of SiO_2 glass up to 100 GPa. Physical
621   Review B, 82, 184102.

622   Shi, R., and Tanaka, H. (2019) Distinct signature of local tetrahedral ordering in the scattering
623   function of covalent liquids and glasses. Science Advances, 5, eaav3194.

624   Shimoda, K., and Okuno, M. (2006) Molecular dynamics study of $CaSiO_3$–$MgSiO_3$ glasses under
625   high pressure. Journal of Physics: Condensed Matter, 18, 6531–6544.

626   Shimomura, O., Yamaoka, S., Yagi, T., Wakatsuki, M., Tsuji, K., Fukunaga, O., Kawamura, H.,
627   Aoki, K., and Akimoto, S. (1984) Multi-anvil type X-ray apparatus for synchrotron
628   radiation. In Materials Research Society Symposia Proceedings Vol. 22, pp. 17–20. Elsevier
629   Science Publishing Company, New York.

630   Silbert, L.E., Ertaş, D., Grest, G.S., Halsey, T.C., and Levine, D. (2002) Geometry of frictionless
631   and frictional sphere packings. Physical Review E, 65, 031304.

632   Skinner, L.B., Barnes, A.C., Salmon, P.S., Hennet, L., Fischer, H.E., Benmore, C.J., Kohara, S.,
633   Weber, J.K.R., Bytchkov, A., Wilding, M.C., and others (2013) Joint diffraction and
634   modeling approach to the structure of liquid alumina. Physical Review B, 87, 024201.

635   Sokolov, A.P., Kisliuk, A., Soltwisch, M., and Quitmann, D. (1992) Medium-range order in glasses:
636   Comparison of Raman and diffraction measurements. Physical Review Letters, 69, 1540–
637   1543.

638   Song, C., Wang, P., and Makse, H.A. (2008) A phase diagram for jammed matter. Nature, 453,
639   629–632.

640   Spera, F.J., Nevins, D., Ghiorso, M., and Cutler, I. (2009) Structure, thermodynamic and transport
641   properties of $CaAl_2Si_2O_8$ liquid. Part I: Molecular dynamics simulations. Geochimica et
642   Cosmochimica Acta, 73, 6918–6936.

643   Susman, S., Price, D.L., Volin, K.J., Dejus, R.J., and Montague, D.G. (1988) Intermediate-range
644   order in binary chalcogenide glasses: The first sharp diffraction peak. Journal of Non-
645   Crystalline Solids, 106, 26–29.

646   Vandembroucq, D., Deschamps, T., Coussa, C., Perriot, A., Barthel, E., Champagnon, B., and
647   Martinet, C. (2008) Density hardening plasticity and mechanical ageing of silica glass under
648   pressure: a Raman spectroscopic study. Journal of Physics: Condensed Matter, 20, 485221.

649   Wakabayashi, D., Funamori, N., Sato, T., and Taniguchi, T. (2011) Compression behavior of
650   densified SiO_2 glass. Physical Review B, 84, 144103.

651   Wang, Y., Sakamaki, T., Skinner, L.B., Jing, Z., Yu, T., Kono, Y., Park, C., Shen, G., Rivers, M.L.,
652   and Sutton, S.R. (2014) Atomistic insight into viscosity and density of silicate melts under
653   pressure. Nature Communications, 5, 3241.

654   Weigel, C., Cormier, L., Calas, G., Galoisy, L., and Bowron, D.T. (2008) Intermediate-range order
655   in the silicate network glasses $NaFe_xAl_{1-x}Si_2O_6$ ($x = 0, 0.5, 0.8, 1$): A neutron diffraction and
656   empirical potential structure refinement modeling investigation. Physical Review B, 78,
657   064202.

658   Wilding, M., Guthrie, M., Kohara, S., Bull, C.L., Akola, J., and Tucker, M.G. (2012) The structure
659   of $MgO–SiO_2$ glasses at elevated pressure. Journal of Physics: Condensed Matter, 24,
660   225403.

661   Wright, A.C. (1994) Neutron scattering from vitreous silica. V. The structure of vitreous silica:
662   What have we learned from 60 years of diffraction studies? Journal of Non-Crystalline
663   Solids, 179, 84–115.

664   Zachariasen, W.H. (1932) The atomic arrangement in glass. Journal of the American Chemical
665   Society, 54, 3841–3851.

666   Zanatta, M., Baldi, G., Brusa, R.S., Egger, W., Fontana, A., Gilioli, E., Mariazzi, S., Monaco, G.,
667   Ravelli, L., and Sacchetti, F. (2014) Structural evolution and medium range order in
668   permanently densified vitreous SiO_2. Physical Review Letters, 112, 045501.

669   Zeidler, A., Wezka, K., Rowlands, R.F., Whittaker, D.A.J., Salmon, P.S., Polidori, A., Drewitt,
670   J.W.E., Klotz, S., Fischer, H.E., Wilding, M.C., and others (2014a) High-pressure
671   transformation of SiO_2 glass from a tetrahedral to an octahedral network: A joint approach
672   using neutron diffraction and molecular dynamics. Physical Review Letters, 113, 135501.

673   Zeidler, A., Salmon, P.S., and Skinner, L.B. (2014b) Packing and the structural transformations in
674   liquid and amorphous oxides from ambient to extreme conditions. Proceedings of the
675   National Academy of Sciences, 111, 10045–10048.

676

677 **FIGURES**

678 **FIGURE 1.** Schematic showing the cell assembly applied for XRD experiments in the pressure

679 region from 7.3 to 12.3 GPa.

680

681 **FIGURE 2.** $S^X(Q)$ (**a**) and $S^N(Q)$ (**b**) of basaltic glass on compression. The inset shows an enlarged

682 view of the low Q region for $S^X(Q)$. The curves below $Q = \sim1.5$ Å^{-1} were not accessible and thus

683 were extrapolated by fitting the Lorentzian function to the FSDP. $S^X(Q)$ in the pressure range from

684 1 atm to 6.0 GPa (Ohashi et al. 2018) are also depicted for comparison.

685

686 **FIGURE 3.** Positions of the FSDP (**a**) and the PP (**b**), and the FWHMs of the FSDP (**c**) and the PP

687 (**d**) under pressure. "Decomp." in the legend stands for decompression. The FWHM values derived

688 from $S^N(Q)$ data for MgSiO$_3$, CaSiO$_3$ (Salmon et al. 2019), and SiO$_2$ (Hattori, personal

689 communication) glasses are also shown for comparison. Vertical errors are originated from

690 Lorentzian multiple-fitting errors. For symbols without error bars, error bars are smaller than the

691 symbol size.

692

693 **FIGURE 4.** $g^X(r)$ (**a**) and $g^N(r)$ (**b**) of basaltic glass at high pressures. $g^X(r)$ in the pressure range

694 from 1 atm to 6.0 GPa are from Ohashi et al. (2018). $g^X(r)$ and $g^N(r)$ at high pressures are shifted

695 vertically by unity. The peaks assigned to the cation-cation correlation are bracketed by the two-

696 way arrows.

697

698 **FIGURE 5.** Pressure dependences of $r_{Si(Al)O}$ and r_{OO} (**a**), $CN_{Si(Al)O}$ and CN_{OO} (**b**), $\Theta_{OSi(Al)O}$ (**c**).

699 "Decomp." in the legend stands for decompression. Vertical errors are originated from Gaussian

700 fitting errors. For symbols without error bars, error bars are smaller than the symbol size.

701

29

702   **FIGURE 6.** Comparison between $S^X(Q)$ (**a**) and $g^X(r)$ (**b**) at ambient pressure, and those under

703   decompression for each high-pressure experiment. "Decomp." in the legend and inset stands for

704   decompression. The inset in **a** shows an enlarged view of the low-Q region for $S^X(Q)$.

705

706   **FIGURE 7.** Pressure dependence of η_O for basaltic and SiO_2 glasses at high pressures. The η_O of

707   SiO_2 glass and the RCP values are from Prescher et al. (2017) and Song et al. (2008), respectively.

708   For symbols without error bars, error bars are smaller than the symbol size.

709

710 **TABLES**

711 **TABLE 1.** X-ray and neutron weighting factors for each i-j atomic pair of basaltic glass

	j = Si	Al	Fe	Mg	Ca	Na	O
$w_{ij}^X(0)$							
i = Si	0.0595						
Al	0.0400	0.0067					
Fe	0.0353	0.0118	0.0052				
Mg	0.0233	0.0078	0.0069	0.0023			
Ca	0.0416	0.0140	0.0123	0.0082	0.0073		
Na	0.0095	0.0032	0.0028	0.0019	0.0033	0.0004	
O	0.2192	0.0736	0.0650	0.0430	0.0766	0.0174	0.2019
w_{ij}^N							
i = Si	0.0214						
Al	0.0129	0.0019					
Fe	0.0156	0.0047	0.0028				
Mg	0.0127	0.0038	0.0046	0.0019			
Ca	0.0119	0.0036	0.0043	0.0035	0.0016		
Na	0.0038	0.0011	0.0014	0.0011	0.0010	0.0002	
O	0.1930	0.0580	0.0702	0.0572	0.0535	0.0171	0.4351

712

713 **TABLE 2.** Values of n, Q_1, Q_2, ΔQ_1, and ΔQ_2 at various pressures

P (GPa)	n (Å^{-3})	Q_1 (Å^{-1})	Q_2 (Å^{-1})	ΔQ_1 (Å^{-1})	ΔQ_2 (Å^{-1})
XRD					
10^{-4}	0.0766(5)	1.959(1)	3.221(8)		
1.72(5)	0.0814	2.011(2)	3.21(1)		
3.31(8)	0.0852	2.059(2)	3.188(6)		
4.73(5)	0.0883	2.114(4)	3.14(2)		
5.95(9)	0.0908	2.153(3)	3.11(1)		
10^{-4} [a]	0.0812	2.015(1)	3.196(7)		
7.25(3)	0.0932	2.190(2)	3.087(8)		

8.99(6)	0.0962	2.204(4)	3.11(2)		
10.3(1)	0.0984	2.262(2)	3.111(8)		
11.2(2)	0.0998	2.276(3)	3.117(9)		
12.3(2)	0.1015	2.315(1)	3.147(4)		
9.46(9) [a]	0.0985	2.263(4)	3.11(1)		
7.44(4) [a]	0.0980	2.253(1)	3.116(2)		
10^{-4} [a]	0.0888	2.110(3)	3.240(8)		
ND					
10^{-4}	0.0766	1.816(3)	2.832(8)	0.87(1)	0.60(3)
2	0.0827	1.865(5)	2.85(1)	0.74(1)	0.68(2)
4	0.0877	1.915(1)	2.855(1)	0.84(1)	0.45(3)
7	0.0926	1.966(8)	2.865(2)	0.92(2)	0.46(2)
9	0.0960	2.065(4)	2.881(2)	0.69(1)	0.59(1)
13	0.1018	2.132(2)	2.933(1)	0.43(2)	0.575(6)
18	0.1092	2.232(4)	3.011(2)	0.31(1)	0.601(9)

Note: Errors on peak positions are originated from Lorentzian fitting errors.

[a] Under decompression. In this condition, number density n was estimated from the pressure dependence of Q_1 during compression (see text).

714

715   **TABLE 3.** Values of $r_{Si(Al)O}$, $CN_{Si(Al)O}$, r_{OO}, CN_{OO}, $\Theta_{OSi(Al)O}$, and η_O at various pressures

P (GPa)	$r_{Si(Al)O}$ (Å)	$CN_{Si(Al)O}$ [b]	r_{OO} (Å)	CN_{OO}	$\Theta_{OSi(Al)O}$ (°)	η_O
XRD						
10^{-4}	1.653(1)	4.59(5)				
1.72(5)	1.644(1)	4.53(6)				
3.31(8)	1.631(1)	4.37(6)				
4.73(5)	1.625(2)	3.98(8)				
5.95(9)	1.647(1)	4.85(5)				
10^{-4} [a]	1.6548(8)	4.98(4)				
7.25(3)	1.640(1)	4.22(5)				
8.99(6)	1.644(1)	4.40(6)				

10.3(1)	1.651(1)	4.53(4)				
11.2(2)	1.610(2)	3.0(2)				
12.3(2)	1.637(1)	3.92(8)				
9.46(9) [a]	1.660(1)	4.27(6)				
7.44(4) [a]	1.647(2)	4.58(5)				
10^{-4} [a]	1.669(1)	4.95(5)				
ND						
10^{-4}	1.6349(4)	3.75(3)	2.652(2)	4.7(1)	108.405(1)	0.4878(9)
2	1.6379(3)	3.80(2)	2.6514(9)	4.8(1)	108.075(2)	0.5284(5)
4	1.6260(7)	3.71(4)	2.6443(7)	6.09(6)	107.679(2)	0.5574(4)
7	1.6267(9)	3.82(6)	2.653(5)	7.7(2)	109.286(3)	0.595(3)
9	1.6393(6)	3.91(7)	2.663(4)	8.0(3)	108.618(3)	0.625(3)
13	1.6129(6)	2.96(5) [c]	2.639(2)	8.6(1)	109.775(6)	0.648(2)
18	1.640(1)	3.25(6) [c]	2.606(8)	8.4(4)	105.250(8)	0.673(6)

Notes: Errors on the *r* values are originated from Gaussian fitting errors. Errors on the *CN* values are based on the error propagation of the fitting errors.

[a] Under decompression. In this condition, number density *n* was estimated from the pressure dependence of Q_1 during compression (see text).

[b] $CN_{Si(Al)O}$ values were calculated as 3.85(5) at 13 GPa and 4.24(6) at 18 GPa by using w_{SiO}^N instead of $w_{SiO}^N + w_{AlO}^N$ (Eq. 3b).

716

717

Figure 2a
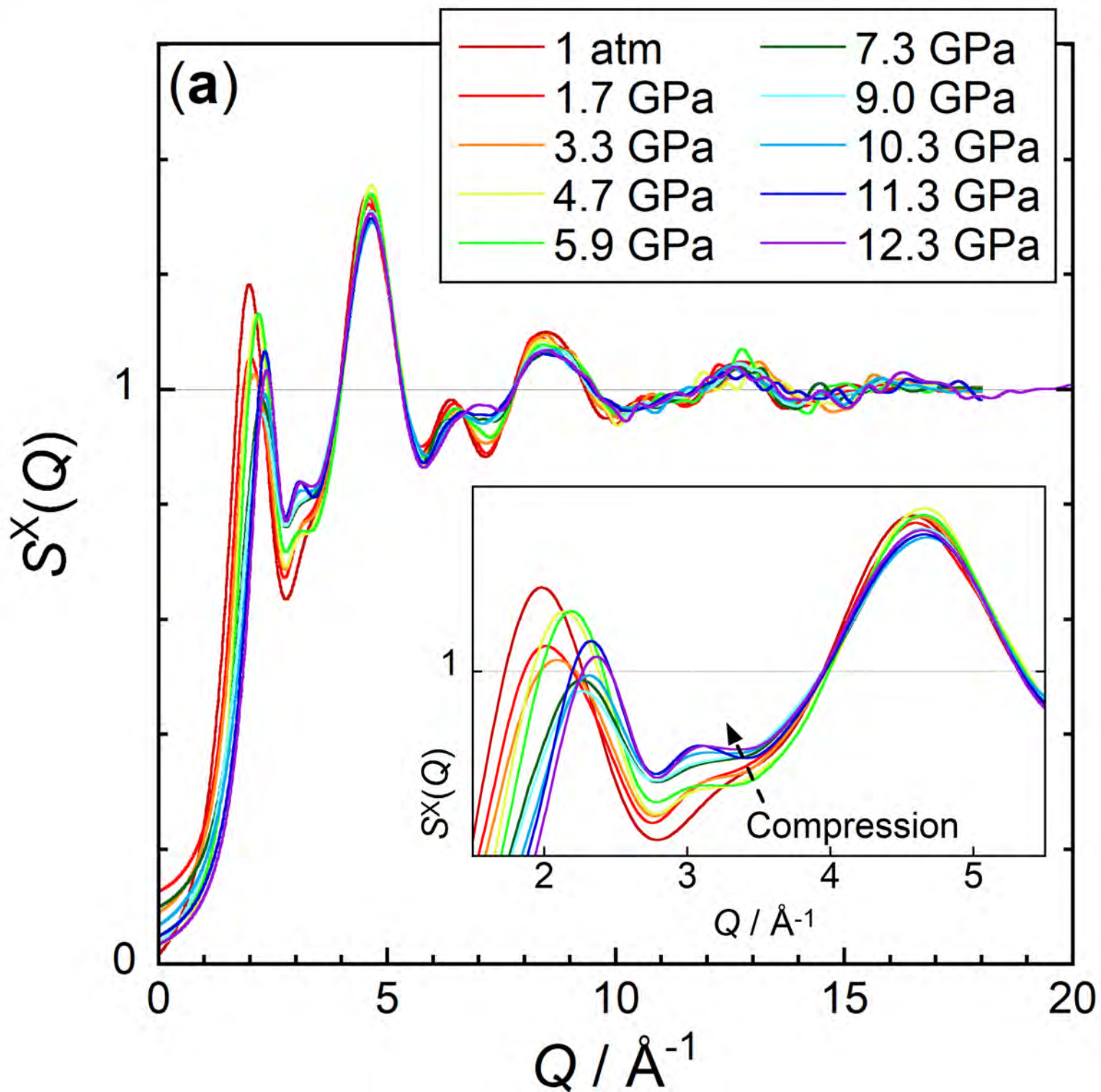
Figure 2b
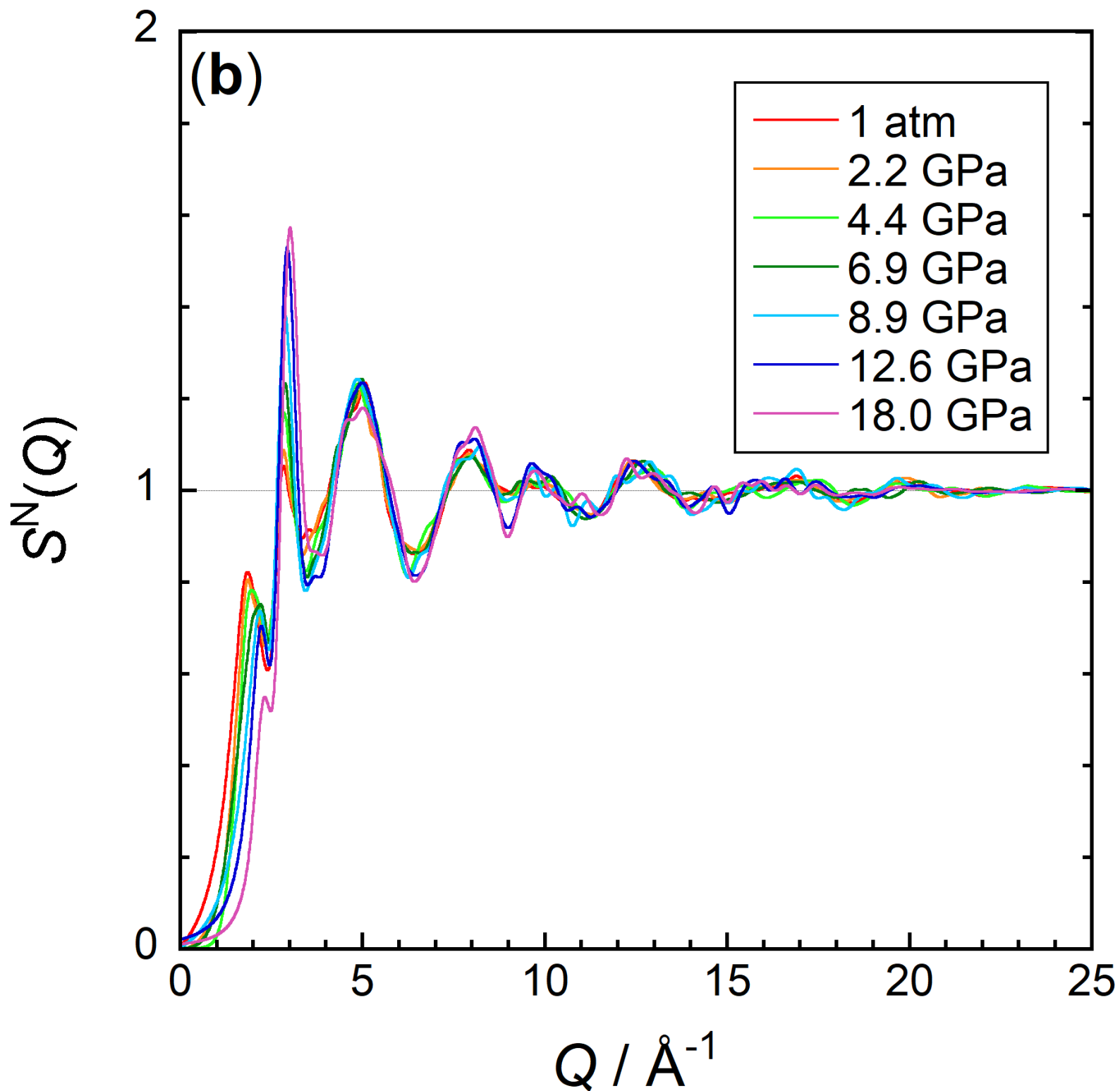
Figure 3a
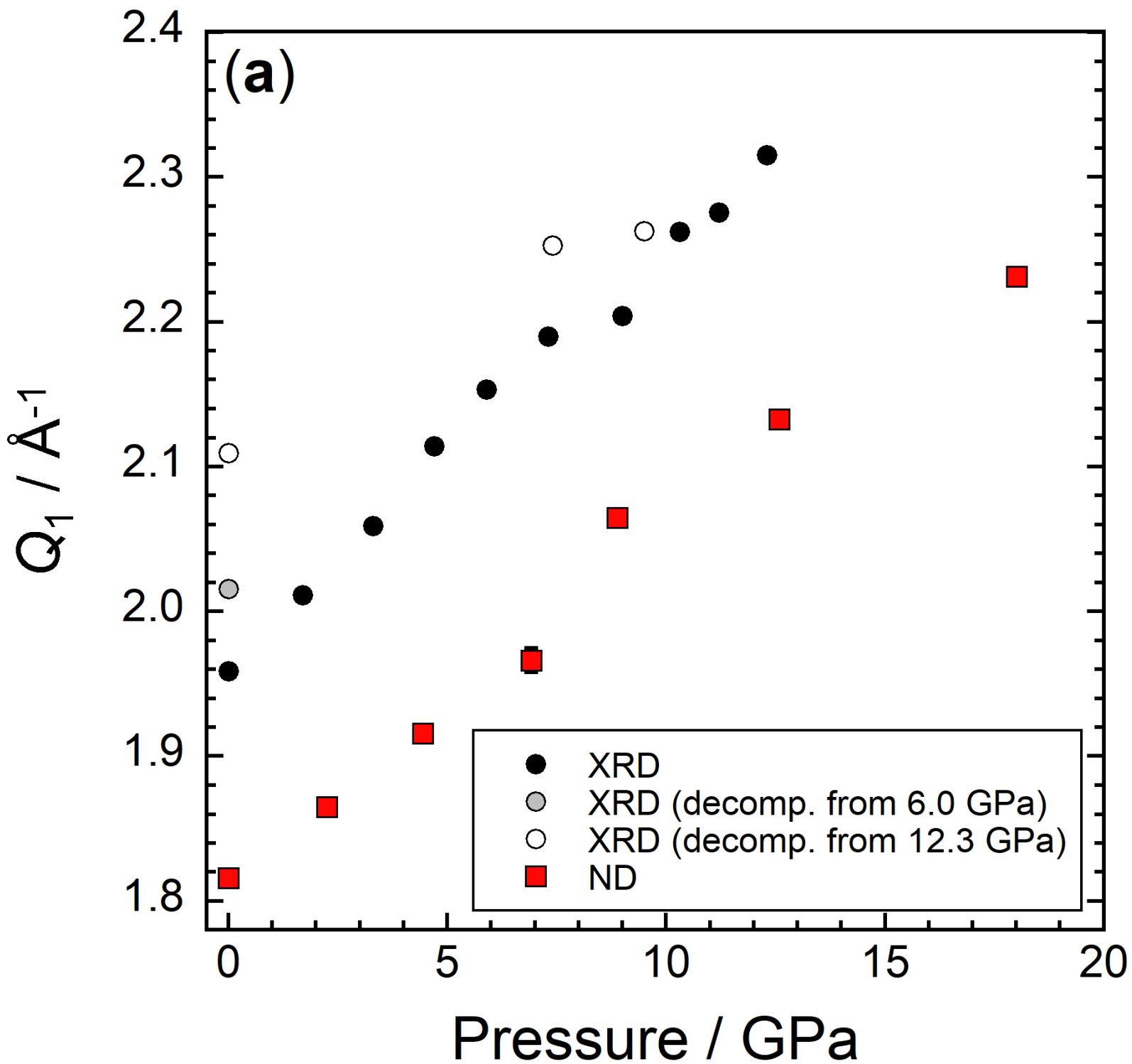
Figure 3b
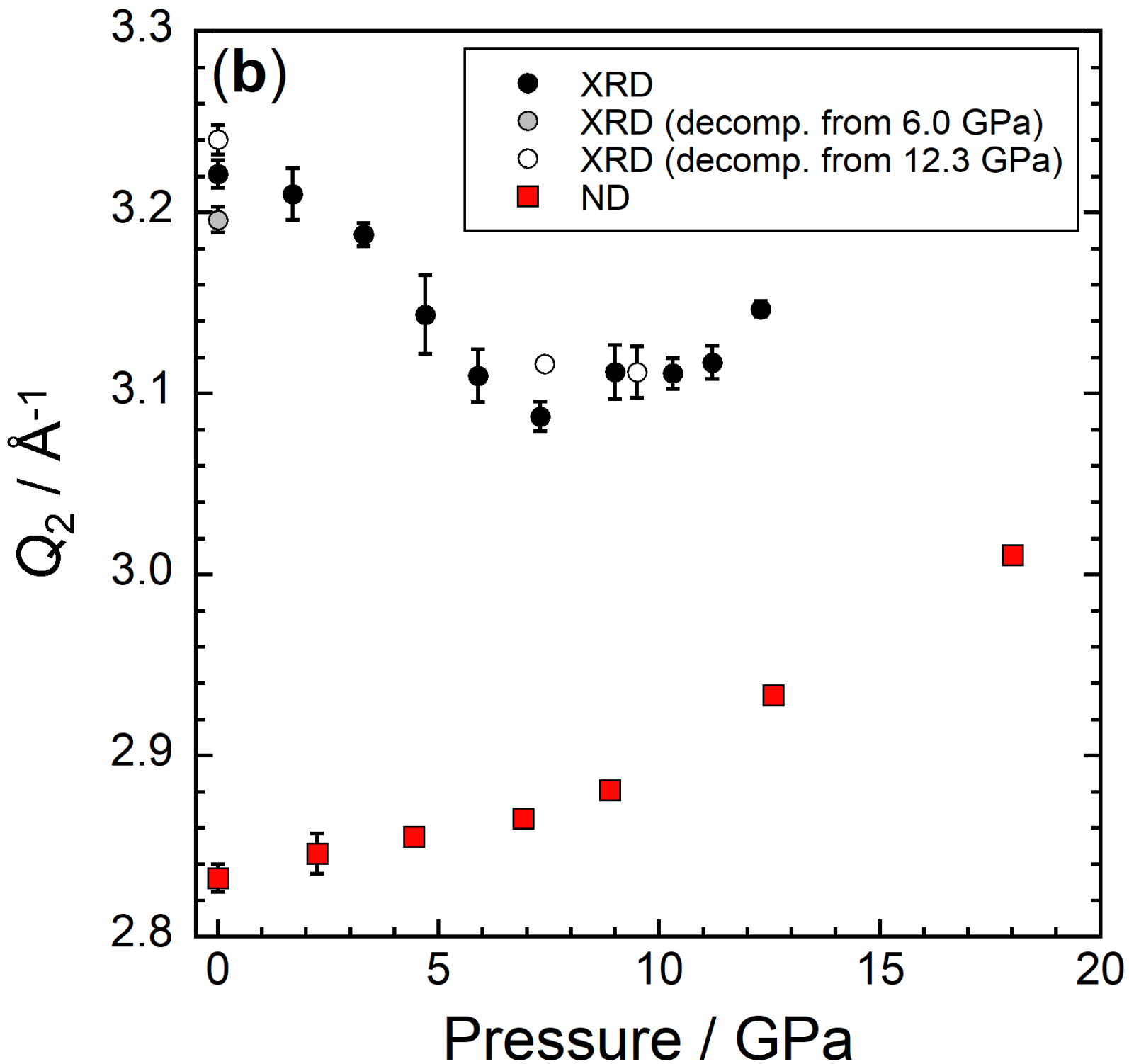
Figure 3c
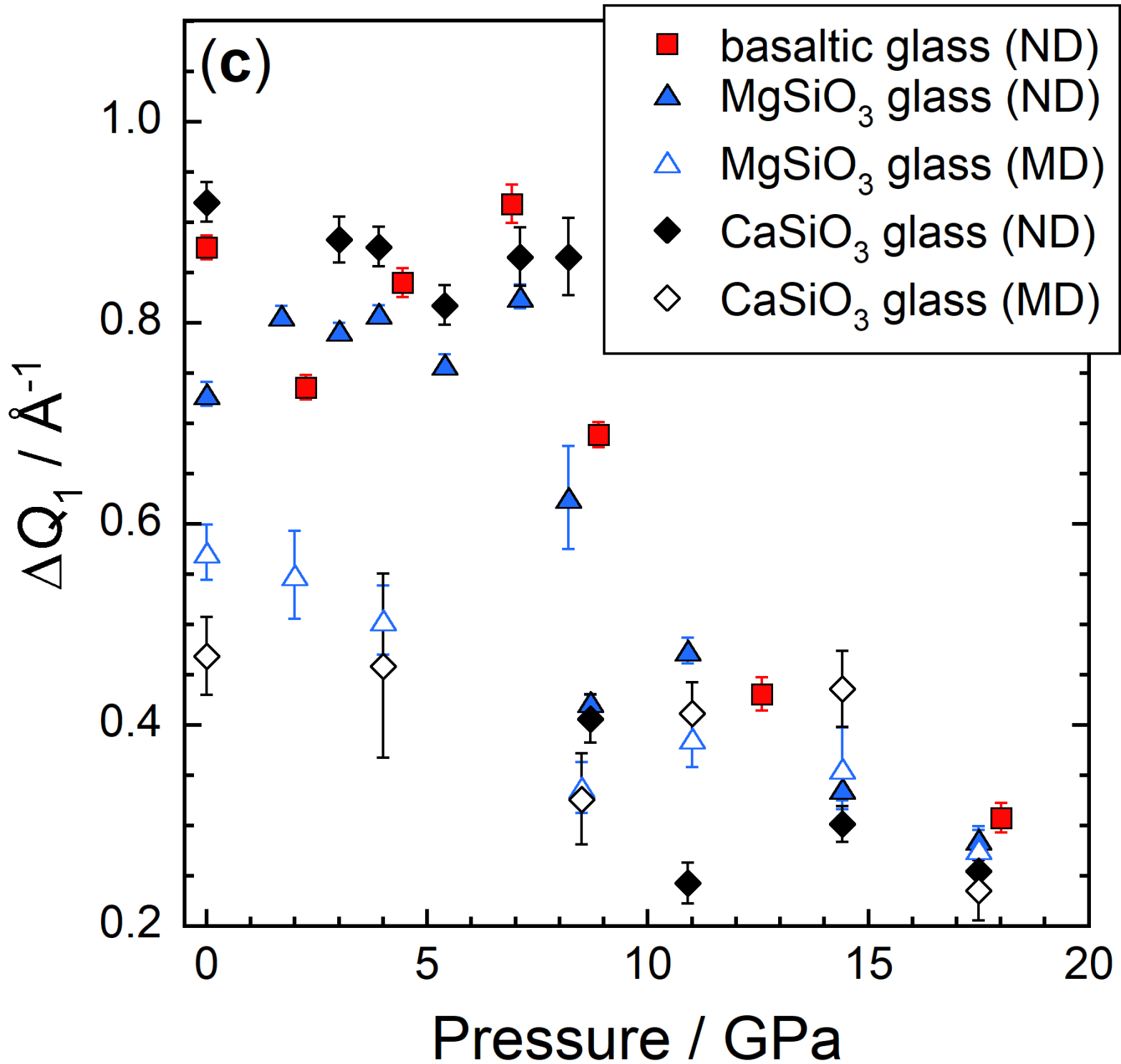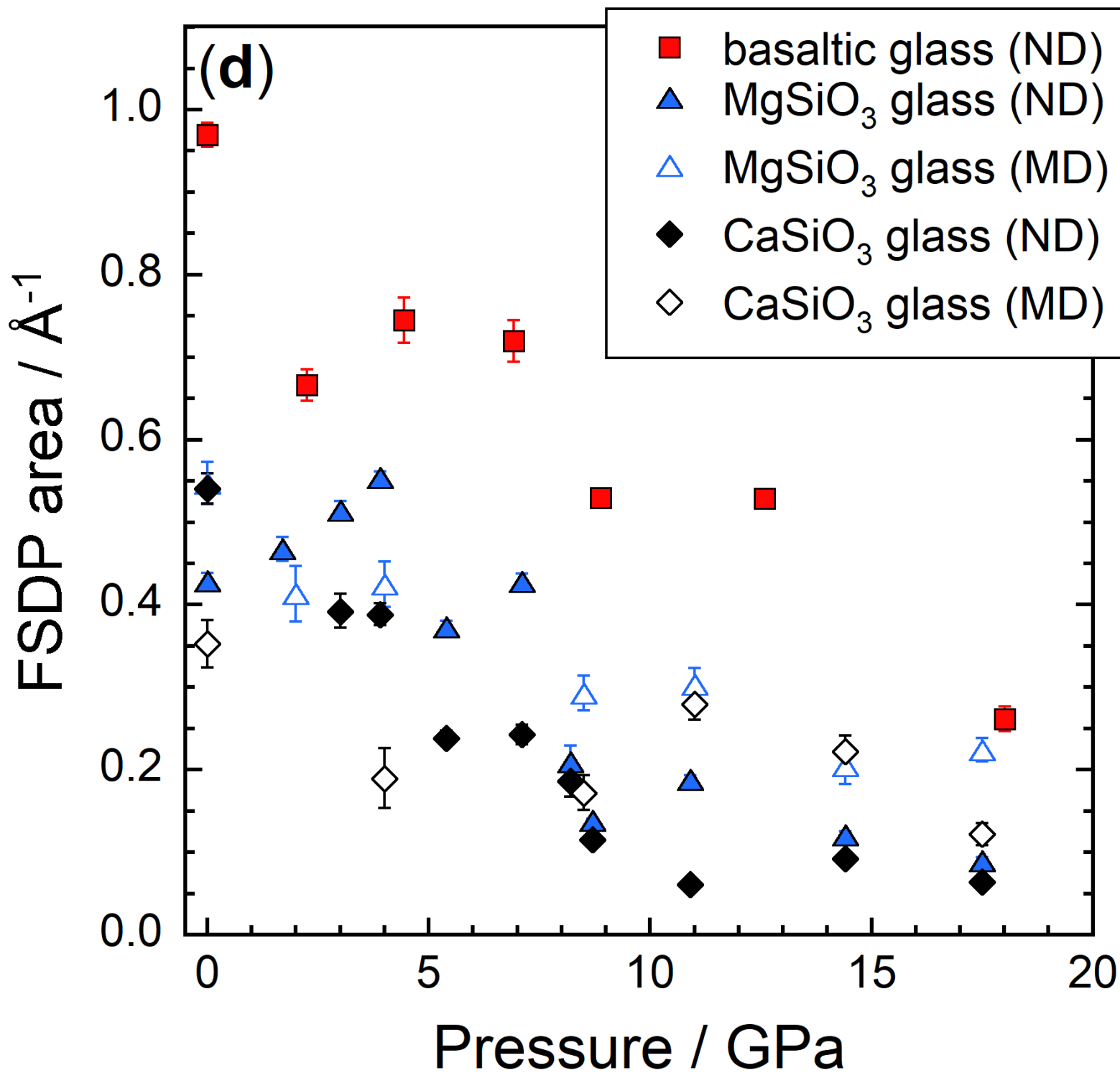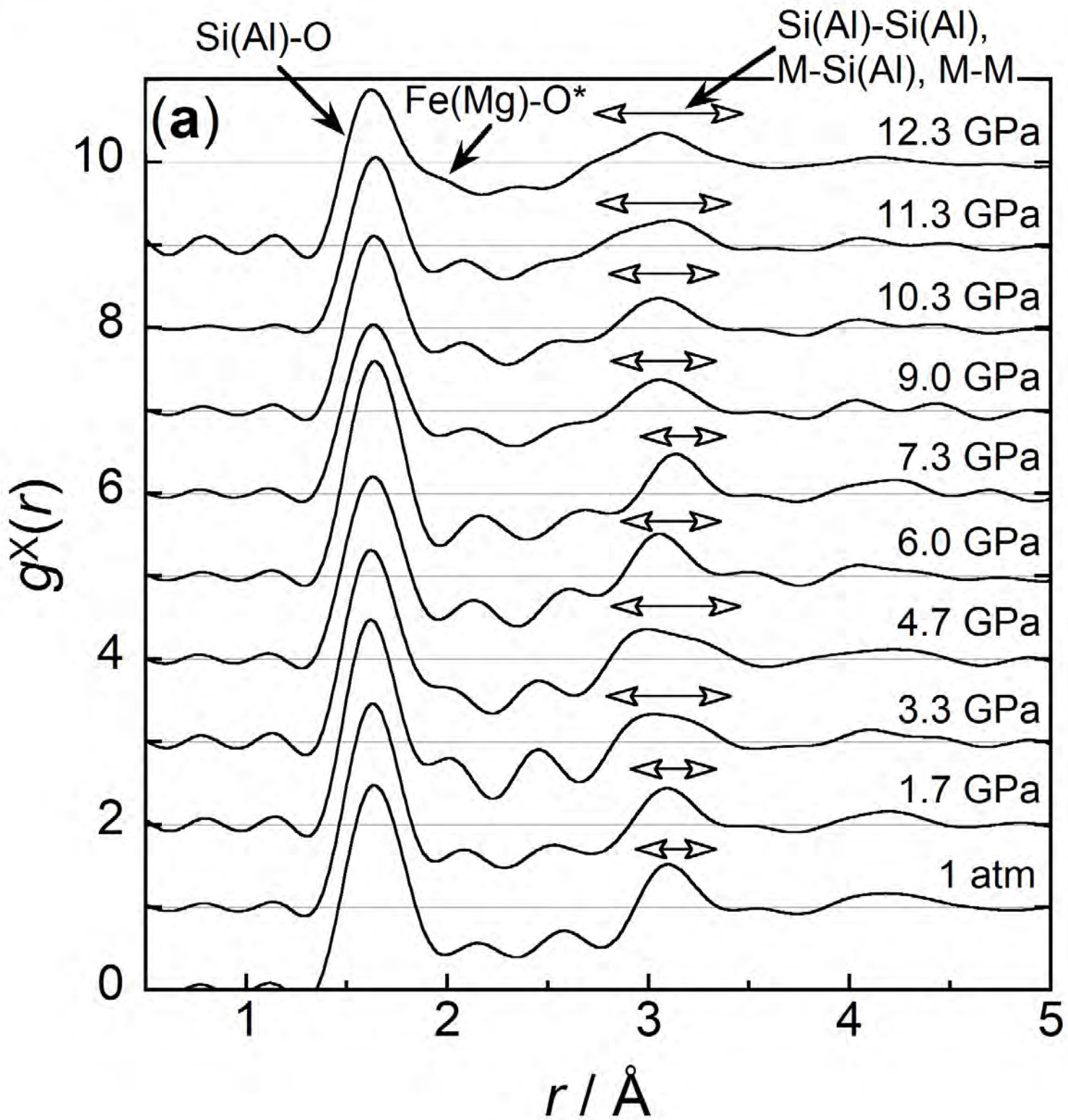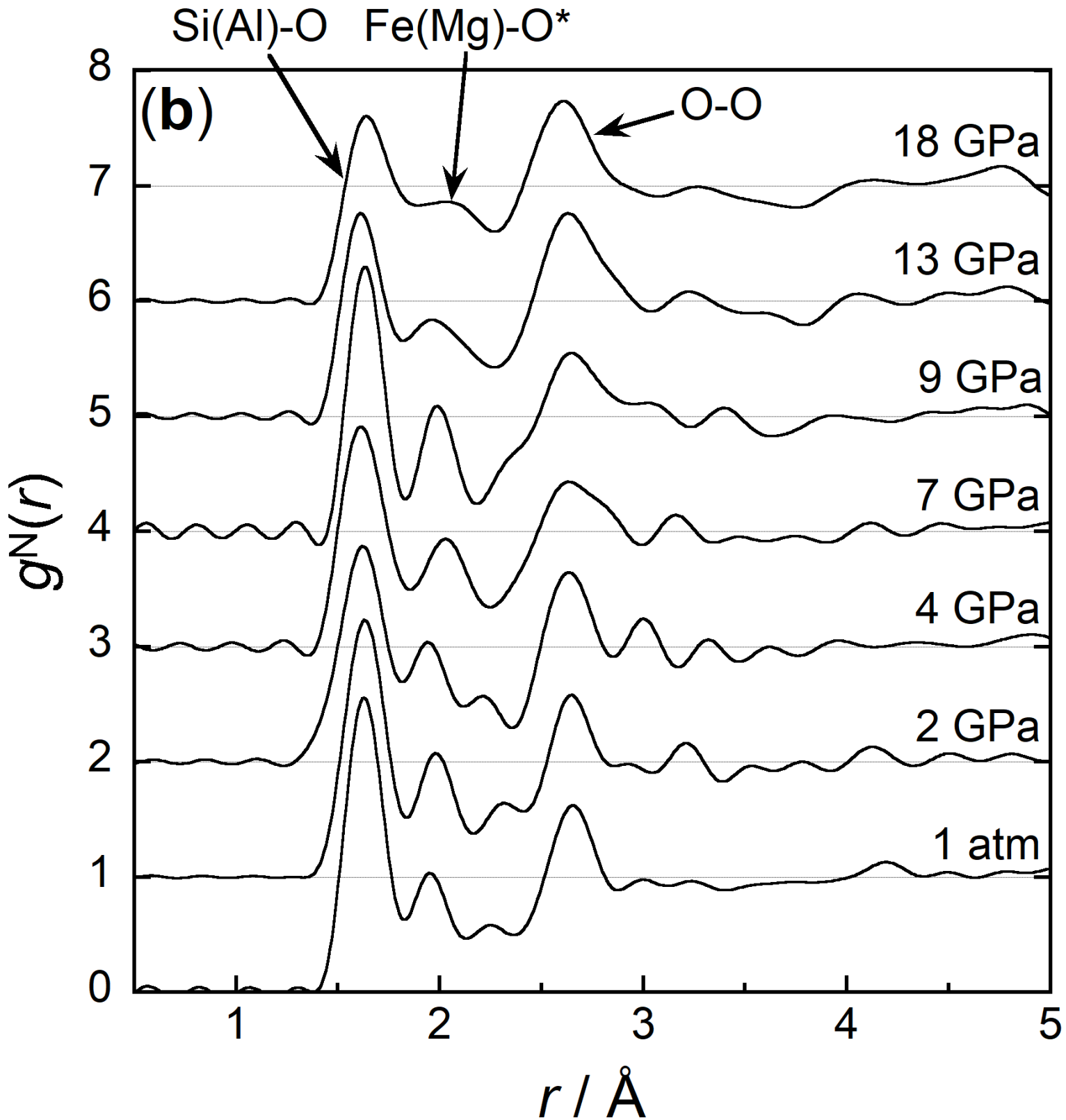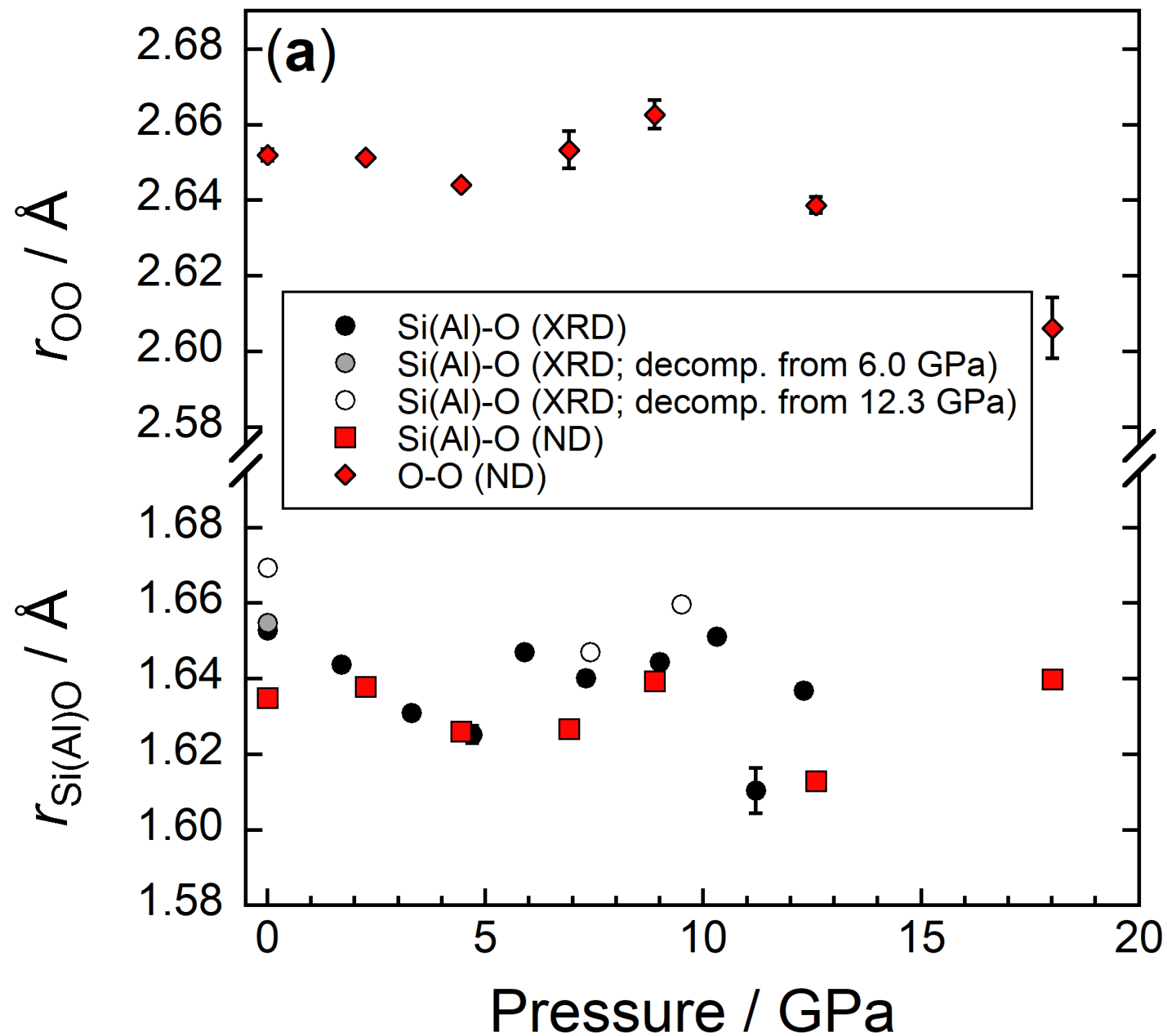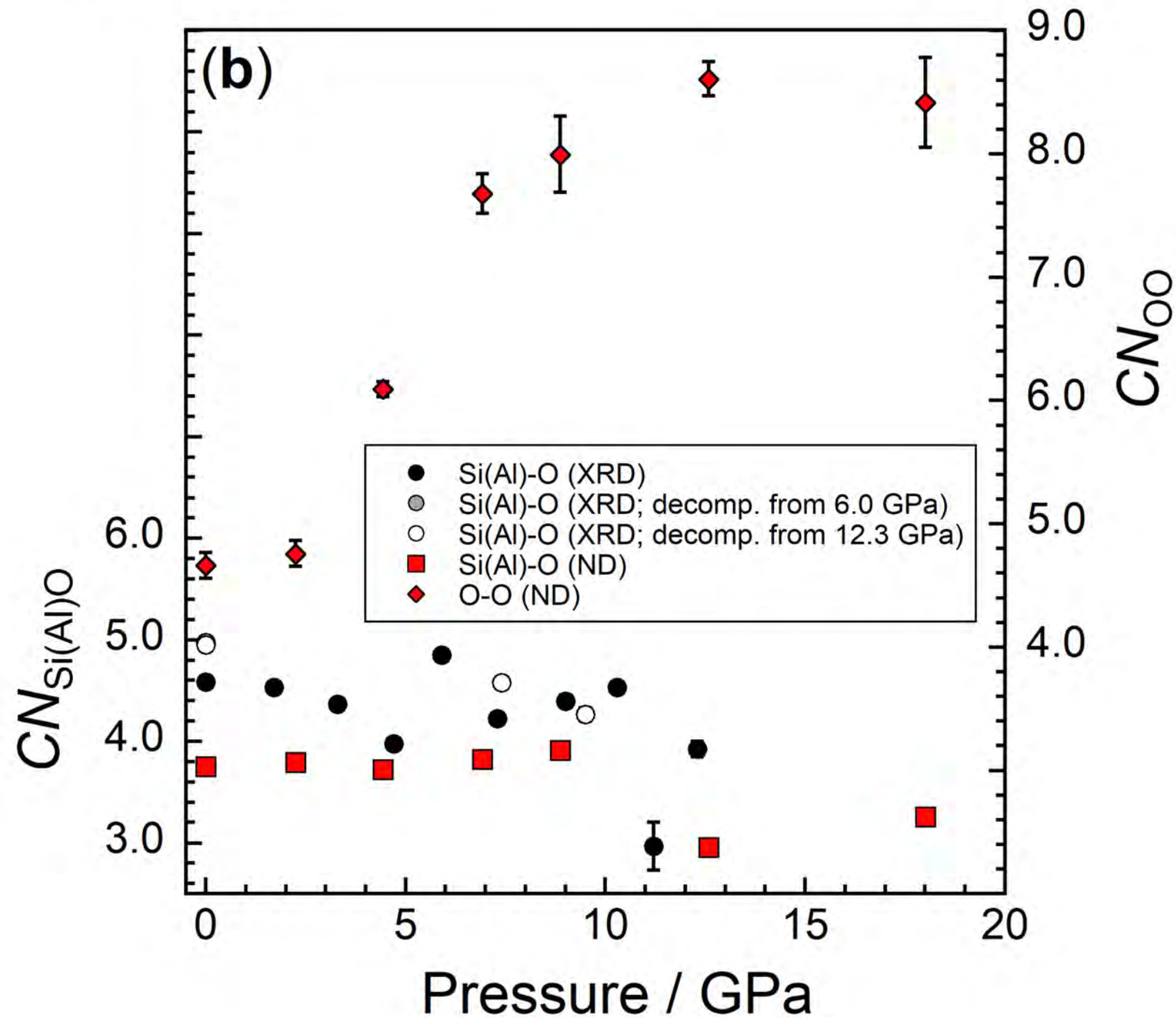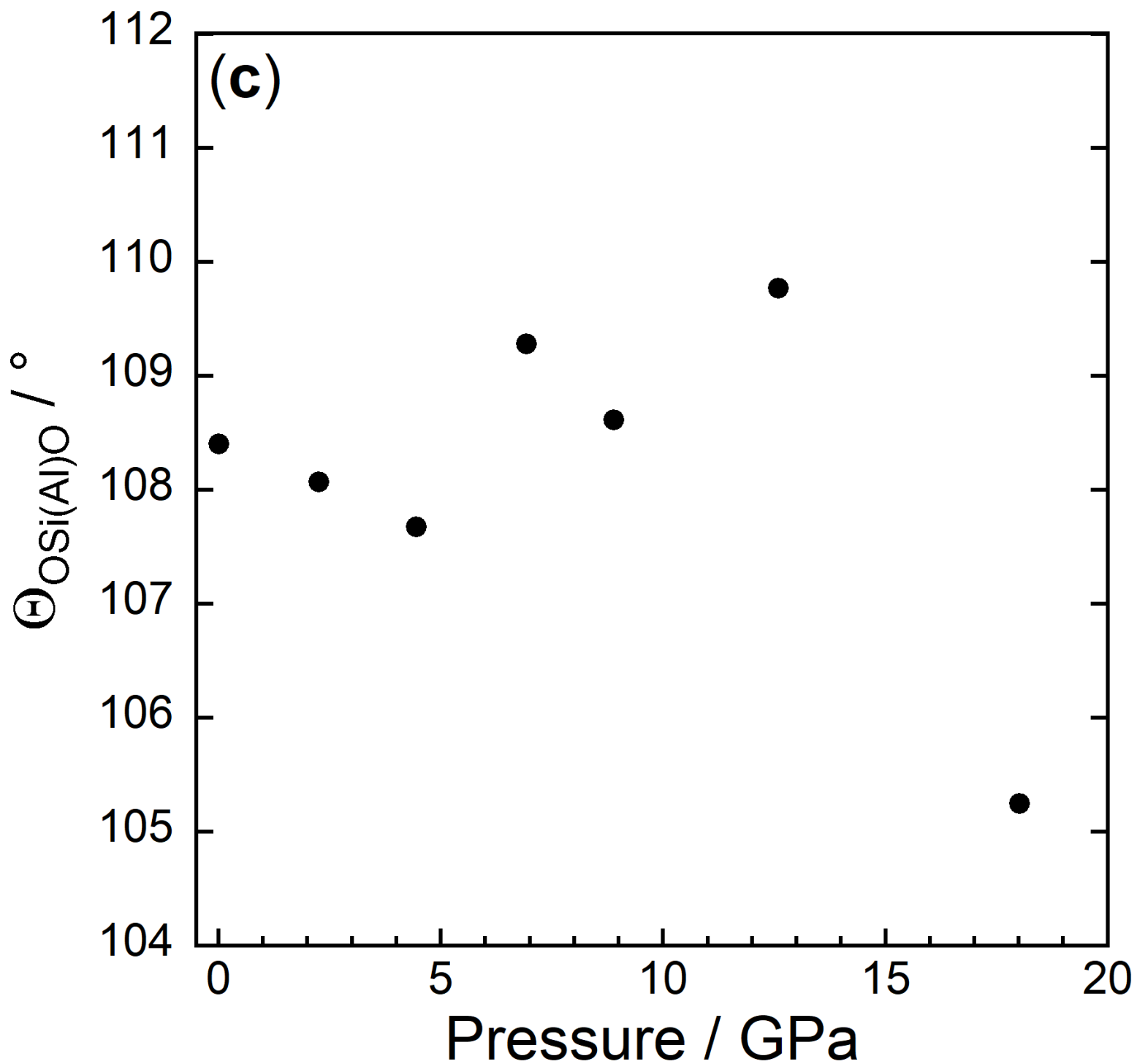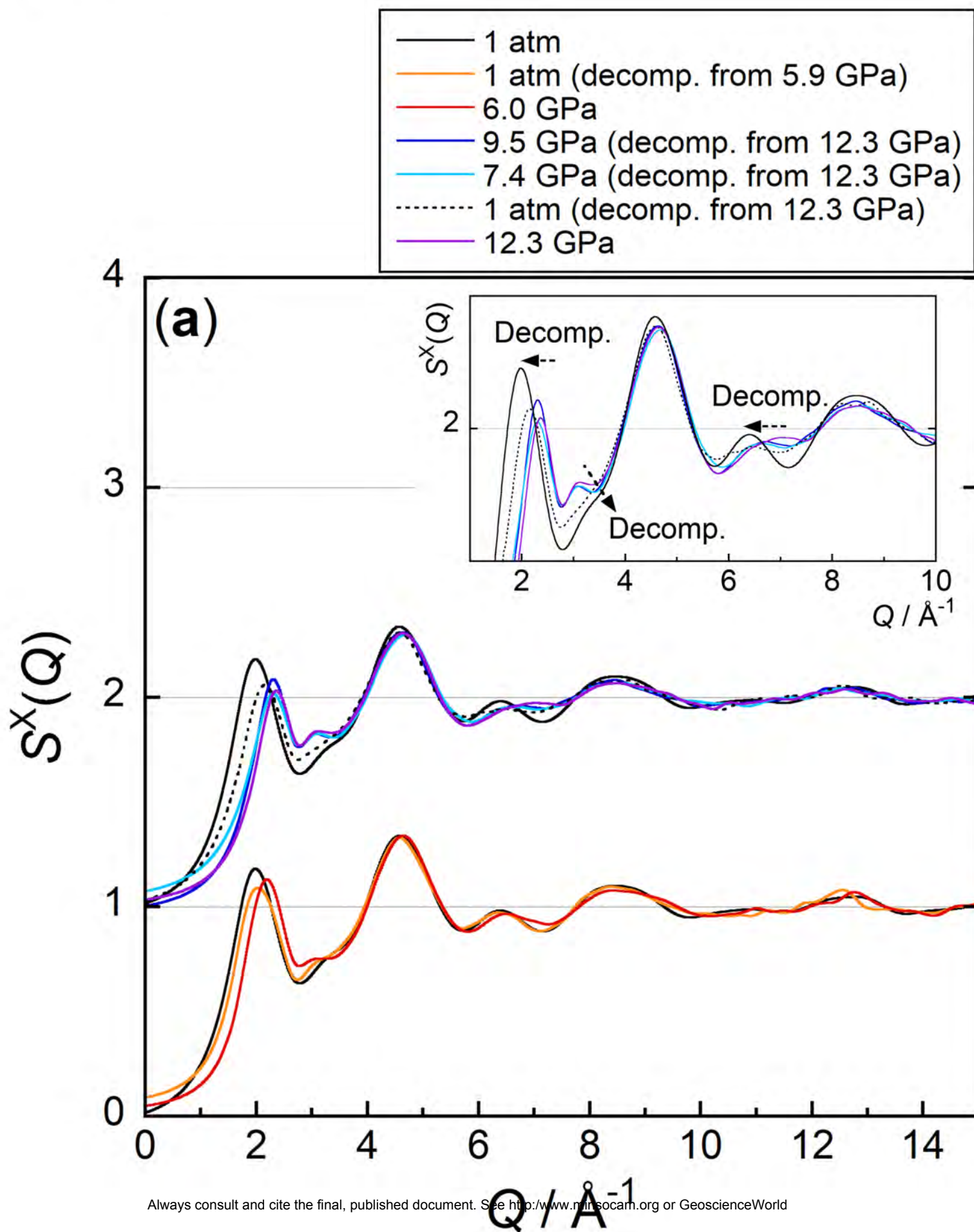
Figure 3d

Figure 4a

Figure 4b

Figure 5a

Figure 5b

Figure 5c

Figure 6a

(a)

Legend:
- 1 atm
- 1 atm (decomp. from 5.9 GPa)
- 6.0 GPa
- 9.5 GPa (decomp. from 12.3 GPa)
- 7.4 GPa (decomp. from 12.3 GPa)
- 1 atm (decomp. from 12.3 GPa)
- 12.3 GPa

Figure 6b

Figure 7